

Warsaw University
Division of Particles and Fundamental Interactions

Mikołaj Ćwiok

**Study of the performance of
Resistive Plate Chamber prototypes**

M.Sc. thesis written under supervision of
dr Maciej Górski ^a
and
prof. dr hab. Jan Królikowski ^b

Warsaw 1996

^a Soltan's Institute for Nuclear Studies, Warsaw

^b Division of Particles and Fundamental Interactions, Warsaw University

Contents

1	Introduction	2
2	LHC physics	3
3	CMS detector	5
3.1	Muon trigger rates	6
3.2	Muon trigger timing	6
3.3	Momentum measurements	6
3.4	RPC performance	6
3.5	Trigger algorithm	7
4	RPC - principle of operation	8
5	Data on the gas mixtures	10
5.1	Specific primary ionisation	10
5.2	Cluster size distribution	10
5.3	Mobility of positive ions	12
5.4	Gain, drift velocity and diffusion	13
6	Simulation with GARFIELD	16
6.1	Geometry	16
6.2	Description of the model	17
6.3	Electron and ion currents	18
6.4	Total and visible charges	19
6.5	Gain and streamer probability	20
6.6	Charge spectra	23
6.7	Timing and effect of diffusion	26
6.8	Effect of varying gap thickness	26
6.9	Effect of varying gas composition	26
6.10	Effect of varying SPI	27
6.11	Effect of varying incident track angle θ	27
7	RPC working model	28
7.1	Single cell	29
7.2	Results on 5×5 cells model	30
7.3	Results on 15×15 cells model	31
8	Experimental setup	34
8.1	Geometry and triggering system	34
8.2	Read-out electronics	34
9	Experimental results	36
9.1	Event classification	36
9.1.1	Small pulse	36
9.1.2	Big pulse, big pulse with precursor	41
9.1.3	Empty event	41
9.2	Amplitude and charge resolutions	41
9.3	Time resolution	41
9.4	Timing properties of small pulses	42
9.5	Amplitude and charge of small pulses	46
9.6	Timing properties of big pulses	50
9.7	Strip multiplicity	52

9.8 Efficiency	55
10 Comparison between simulation and experiment	58
11 Conclusions	58

1 Introduction

In recent years Resistive Plate Chambers are used in many experiments demanding good space and time resolution and large detection area [1].

The main features of the RPCs are:

- fast response time (~ 10 ns) and good time resolution (~ 2 ns)
- simple construction and low cost of mass production.

RPCs are suitable detectors for future hadronic colliders and for cosmic rays physics. One of the largest applications will be CMS and ATLAS detectors for the Large Hadron Collider, planned to be built at CERN.

However, the main drawbacks of this detectors is their rate capability when operated in the streamer mode (classical RPCs). The efficiency falls below 90% when incoming particles flux exceeds 100 Hz/cm^2 . In order to improve the efficiency chambers have to be operated at lower gains to prevent streamer discharges (avalanche mode). It is believed that a suitable gas mixture together with pre-amplifiers mounted to the read-out strips will allow to use RPCs for particle fluxes of about 1500 Hz/cm^2 without efficiency loss.

Apart from rate problems there is a lack of understanding the chamber response from the basic principles, eg. starting from the nature of the used gas, and ending on the signals induced on pick-up strips.

The aim of this thesis is to help understand the chamber performance in the avalanche mode of operation.

This work is divided into simulation and experimental part:

1. simulation of the RPC response using available program packages and experimental data
2. results on tests with RPC prototype assembled in Warsaw¹

In Section 2 an introduction to LHC physics is presented. In Section 3 the CMS detector is described with emphasis on the RPC-based muon trigger system, for developing which the Warsaw group is partially responsible.

The basic information about construction and operation of the RPCs are presented in Section 4.

Sections 5, 6 and 7 are dedicated to simulation of the RPCs performance. In Section 5 gas properties were derived from data found in the literature as well as from predictions of MAGBOLTZ [15] and HEED [16] programs.

Avalanches in gases were simulated using GARFIELD program [12] in Section 6.

A working model of RPC was proposed in Section 7. Signals induced on pick-up strips were simulated with SPICE program, using discharges in the gas gap generated with GARFIELD.

Experimental setup and measurements are discussed in Sections 8 and 9, respectively.

Finally, a comparison between simulation and experiment is discussed in Section 10, and conclusions are presented in Section 11.

¹The Detector Laboratory of the Institute of Experimental Physics, Warsaw.

2 LHC physics

The Large Hadron Collider (LHC), planned to be build at CERN in Geneva, is a machine designed to collide protons at the centre of mass energy $\sqrt{s} = 14$ TeV.

It is dedicated to test the electroweak sector of the Standard Model (SM) as well as its extension to the Minimal Supersymmetric Standard Model (MSSM). The physics phenomena accessible at energies of about 1 TeV per constituent can be studied.

In addition LHC will be able to collide heavy ions (Pb) with beam energy of 2.76 TeV/nucleon. The LHC design parameters are listed in Table 1 [2].

		Collided particles	
		p-p	Pb-Pb
Beam energy	[TeV]	7	574
Luminosity	[cm ⁻² s ⁻¹]	10 ³⁴	2·10 ²⁷
Time between collisions	[ns]	25	135
Particles per bunch		10 ¹¹	10 ⁷
Circumference	[km]	26.659	
Dipole field	[T]	8.4	

Table 1: LHC parameters.

Four beam intersection points will be provided: two for CMS and ATLAS detectors at high luminosity, and two for LHC-B (dedicated to CP-violation in the B sector) and ALICE (dedicated to heavy ion collisions) detectors at lower luminosity.

The main task for CMS and ATLAS detectors is to discover the Higgs boson predicted by SM theory. The Spontaneous Symmetry Breaking (SSB) mechanism explains non-zero masses of W, Z bosons, but assumes existence of additional scalar, neutral boson. The searches for MSSM Higgs particles will be performed as well. Although theory do not predict mass of the Higgs particle(s) it is expected to be < 1 TeV².

The following searches will be performed at LHC:

1. Standard Model Higgs boson search {H} for m_H mass up to 1 TeV:
 - $H \rightarrow \gamma \gamma$, two photon decay, $m_H = 95 - 150$ GeV
 - $H \rightarrow Z Z^*$, $Z Z \rightarrow 4\ell^\pm$, four charged leptons decay ($\ell = e, \mu$), $m_H = 135 - 525$ GeV
 - $H \rightarrow Z Z \rightarrow \ell \ell \nu \nu$, $m_H > 500$ GeV
 - $H \rightarrow W W \rightarrow \ell \nu + 2 \text{ jets}$, $H \rightarrow Z Z \rightarrow \ell \ell + 2 \text{ jets}$, heavy Higgs, $m_H \approx 1$ TeV
2. MSSM Higgs bosons search {h⁰, H⁰, A⁰, H[±]} for wide range of $\tan \beta$ and m_A parameters:
 - $h^0, H^0 \rightarrow \gamma \gamma$
 - $h^0, H^0, A^0 \rightarrow \tau \tau \rightarrow \ell^\pm + \text{hadron}^\pm + X$
 - $h^0, H^0, A^0 \rightarrow \mu \mu$
 - $H^0 \rightarrow Z Z^*, Z Z \rightarrow 4\ell^\pm$
 - $h^0 \rightarrow Z Z \rightarrow 4\ell^\pm$
 - $A^0 \rightarrow Z h^0 \rightarrow \ell \ell b \bar{b}$
 - $t \rightarrow H^\pm b, H^\pm \rightarrow \tau \nu_\tau c s$

²Perturbation theory fails when Higgs mass exceeds 1 TeV. Present experiments limit the SM Higgs mass to $m_H > 64$ GeV.

3. Supersymmetric (SUSY) particles searches: squarks, sleptons, gluinos, higgsinos, winos and zinos
4. Heavy flavour physics, in the first phase of LHC operation at low luminosity, $\mathcal{L} = 10^{32} \text{ cm}^{-2} \text{ s}^{-1}$
 - precise measurements of top quark mass and decay channels,
 - CP-violation in the B sector
 - measurement of unitarity triangle angles α, β, γ :
 $\sin 2\alpha$ from $B_d^0 \rightarrow \pi \pi$ channel
 $\sin 2\beta$ from $B_d^0 \rightarrow J/\psi K_S^0$ channel
 - determination of the mixing parameter χ_s from $B_s^0 - \overline{B}_s^0$ oscillations
5. Heavy ion physics: suppression of Υ', Υ'' production, relative to Υ , due to formation of quark-gluon plasma.

3 CMS detector

The Compact Muon Solenoid (CMS) is a general purpose detector for LHC machine [3]. It will precisely measure muons, electrons and photons over wide energy range. It consists of: inner tracker, calorimeters and muon detection systems (Figure 1). The inner tracker, electromagnetic and hadron calorimeters in the barrel are contained inside large superconductive solenoid ($R=3$ m, $L=13$ m) that creates 4 T magnetic field. The iron yoke returns magnetic flux outside the coil and is interleaved with 4 muon stations. Each muon station will be equipped with: drift tubes (DT) and resistive plate chambers (RPC) in the barrel, and cathode strip chambers (CSC) and RPCs in the endcaps. The barrel muon detector covers pseudorapidity³ region $|\eta| < 1.3$ and the endcap detector covers $0.9 < |\eta| < 2.4$ (Figure 2).

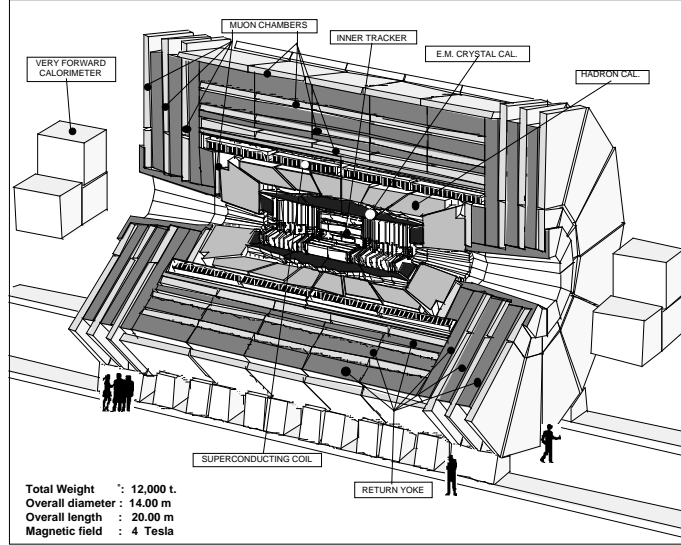


Figure 1: Layout of the CMS detector.

The inner tracker ($R=1.3$ m, $L=6$ m) consists of silicon pixel, silicon strips and Microstrip Gas Chambers (MSGC). Its purpose is to reconstruct high p_t tracks (isolated or within jets) over pseudorapidity range $|\eta| < 2.6$.

The electromagnetic calorimeter (ECAL) covers pseudorapidity range $|\eta| < 1.56$ in the barrel and $1.65 < |\eta| < 2.6$ in the endcaps. Modules made of lead tungstate crystals (PbWO_4) of $25X_0$ ⁴ length will be used as an absorber and active material.

The hadronic calorimeter system consists of hadron calorimeter (HCAL) and very forward calorimeter (VF). HCAL covers $|\eta| < 3$, with granularity that matches ECAL and muon system segmentation up to $|\eta| < 2$. The copper layers (absorber) are interleaved with scintillators (active material). The depth for hadron shower containment in the barrel ranges from 5.46λ ⁵ ($\eta = 0$) to 10.82λ ($|\eta| = 1.3$) and in the endcaps is about 11λ . Additional contributions come from ECAL, coil and Tail Catcher.

The VF calorimeter covers $3 < |\eta| < 5$ region. It must withstand high radiation during LHC operation, therefore it consists of quartz fibres (active material) embedded in iron or copper absorber (10.5λ in total).

³ pseudorapidity $\eta = -\ln \tan \frac{\theta}{2}$.

⁴ X_0 is the radiation length of the absorber.

⁵ λ is the nuclear interaction length of the absorber.

The Warsaw group in CMS collaboration is responsible for RPC-based muon trigger electronics.

3.1 Muon trigger rates

At the LHC two proton bunches will collide every 25 ns, and about 20-30 pp interactions will occur at desired luminosity $\mathcal{L} = 10^{34} \text{cm}^{-2} \text{s}^{-1}$. The main task of the first level trigger is to reduce this 1 GHz rate to 20-30 kHz acceptable by the second level trigger. The muon trigger, one of the first level trigger components, should reduce event rate to ~ 6 kHz. This can be achieved if the trigger system is capable of measuring muon momentum quite precisely, and to apply a sharp p_t cut (few GeV to 100 GeV).

3.2 Muon trigger timing

The identified muon must be assigned to a given bunch crossing. An ambiguity may occur from DT and CSC information only (long drift time $40 \div 160$ ns, long strips or wires). RPCs will be used for trigger purpose because of their very good timing properties (intrinsic time jitter below 15 ns, $\sigma \sim 2$ ns) which allow use of trigger gates shorter than 20 ns.

3.3 Momentum measurements

The magnetic field bends track in $r\phi$ plane as is schematically shown in Figure 3. In order to determine the transverse momentum p_t of the track, the RPC hit pattern in 4 muon stations will be compared to predefined set of patterns by the Pattern Comparator Trigger device (PACT).

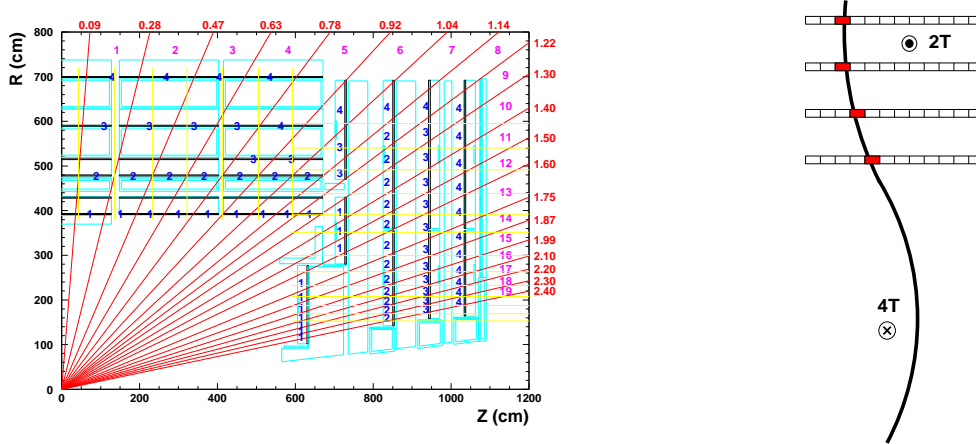


Figure 2: The muon trigger segmentation in η ($\Delta\eta \approx 0.11$). The $\frac{1}{4}$ of the detector is shown. Four muon stations are indicated with numbers: 1, 2, 3, 4.

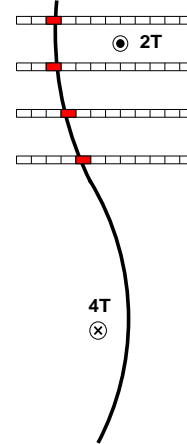


Figure 3: Measurement of p_t of the track based on hits in four muon stations.

3.4 RPC performance

RPCs are equipped with strips parallel to the beam axis in the barrel and radial in the endcaps (projective geometry in ϕ). The strip granularity depends on required momentum resolution (measuring momentum up to 50–100 GeV, optimal $\Delta\phi = 5/16^\circ$), and time spread < 5 ns (time of flight for different η , signal propagation time along strip, optimal $\Delta\eta \approx 0.1$). The length of the strips does not exceed 1 m, and the minimal strip width is 2-3 cm in the innermost barrel station.

The expected hit rate is < 20 Hz/cm² in the barrel and < 700 Hz/cm² in the endcaps. Because coincidence of 4 (or 3) planes is required by the trigger, each chamber must be very

efficient, namely, 98% in the barrel for 100 Hz/cm² rate and above 95% in the endcaps for 1500 Hz/cm² rate. To achieve high efficiency multigap chambers will be used.

A minimum ionising particle may cause more than one hit in an RPC chamber (strip with signal that passed discriminator threshold). Average strip multiplicity have to be less than 2, and fraction of events with more than 4 adjacent hits must not exceed 1%.

In total, RPCs will cover area of 3400 m² in CMS, and pseudorapidity range $|\eta| < 2.1$ (future upgrade to $|\eta| < 2.4$ is possible). About 200.000 channels will be read-out.

3.5 Trigger algorithm

The group of 8 strips in ϕ direction in a single station is called segment ($\Delta\phi = 2.5^\circ$). Segments of the same η from four muon stations are combined with one tower ($\Delta\eta \approx 0.1$ and $\Delta\phi = 2.5^\circ$). Segments of the same η are grouped with one ring.

A fast, dedicated electronics will select⁶ maximum four muons of the highest p_t and will send this information to the global trigger.

⁶The search will be performed at first in each tower, than in rings.

4 RPC - principle of operation

The Resistive Plate Chambers are the gaseous detectors. Their principle of operation is based on the ionisation caused by incident charged particle. The average energy loss per unit length is given by the Bethe-Bloch formula:

$$\frac{dE}{dx} = -K z^2 \frac{Z}{A} \frac{\rho}{\beta^2} \left[\frac{1}{2} \ln \frac{2m_e c^2 \beta^2 \gamma^2 T_{\max}}{I^2} - \beta^2 - \frac{\delta}{2} \right]$$

where

- T_{\max} – maximum energy transfer allowed in each interaction
- $$T_{\max} = \frac{2m_e c^2 \beta^2 \gamma^2}{1 + 2\gamma m_e/M + (m_e/M)^2}$$
- $K = 4\pi N_A r_e^2 m_e c^2$ – constant
- N_A – Avogadro's number
- m_e, r_e – electron mass and classical electron radius
- Z, A – atomic number and atomic mass of the medium
- ρ – density of the medium
- I – mean excitation energy of the medium
- z – charge of incident particle (in e_0 units)
- M – incident particle mass
- β – incident particle velocity (in c units)
- δ – density effect correction.

Usually relativistic particles (eg. cosmic ray muons) are minimum ionising particles, and their energy loss is close to the minimum of $dE/dx(\beta\gamma)$ distribution ($\beta\gamma = 3 \div 4$ region).

In a typical RPC two parallel electrodes made of high resistivity material (bakelite, melamine of $\rho=10^{10 \div 12} \Omega\text{cm}$) generate intense, uniform electric field in a few millimeter gas gap. Usually RPCs are operated at the reduced electric field $E/p \sim 20 \div 50 \text{ Vcm}^{-1}\text{Torr}^{-1}$, while in Multiwire Proportional Chambers and Drift Tubes $E/p < 10 \text{ Vcm}^{-1}\text{Torr}^{-1}$.

External sides of electrodes are covered with the graphite layer (surface resistivity $\sigma \sim 100 \text{ k}\Omega/\square$) which distribute the high voltage across the plane. The electrodes are insulated with thick PVC foils. A cross-section of the RPC prototype tested in this thesis is shown in Figure 4.

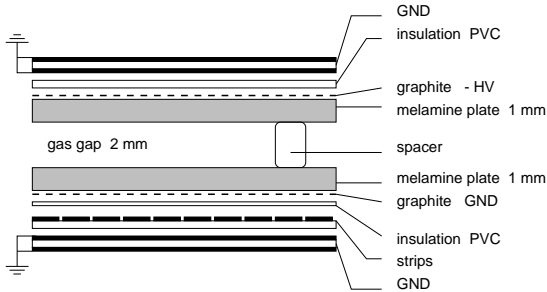


Figure 4: Cross section view of tested RPC prototype.

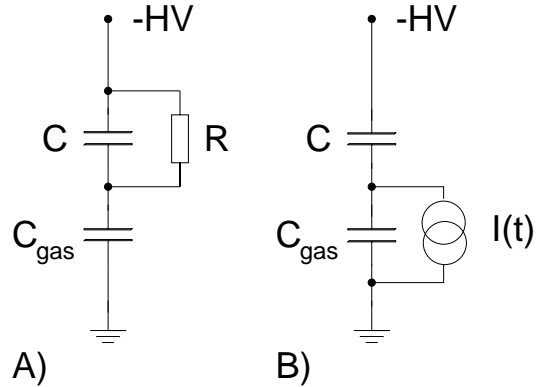


Figure 5: Simple working model of RPC:
A) restoring electric field in the gas gap
B) discharge in gas as a current source.

The primary electron-ion pair created in an ionisation act drifts in electric field. When electrons gain sufficient energy to ionise gas molecules during the time between collisions, the number of charge carriers $n(x)$ increases with drift distance x . The process of avalanche growth is described by the Townsend formula:

$$n(x) = n_0 \exp\left(\int_{x_0}^x \alpha(x') dx'\right)$$

where

$$\begin{aligned} n_0 & - \text{number of primary electrons} \\ \alpha & - \text{first Townsend coefficient.} \end{aligned}$$

The discharge in the gas is read-out by strips or pads pressed to the electrode surface.

Because of resistive electrodes the chamber can be divided into small, independent cells. Locally electric field decreases during ~ 10 ns discharge in one of the cells (Figure 5 b) and electrodes behave like insulators. The resistive plates need time of ~ 10 ms to restore the field (Figure 5 a). The area of an elementary cell is proportional to the charge released in the gas. In order to avoid efficiency loss at high incident particle flux, the chamber must be operated at relatively small gains.

The choice of gas is of great importance for RPC operation. Usually chamber is filled with mixture of: argon, hydrocarbons and freon at atmospheric pressure. The hydrocarbon molecules absorb UV photons and prevent propagation of discharge in the whole chamber. The electronegative freon molecules capture electrons and reduce avalanche size.

The tested RPC prototype (Figure 4) had active area of 20×20 cm². It consisted of two 1 mm thick melamine plates, 2 mm gas gap with two spacers of $\phi=1$ cm. External surfaces of the electrodes were covered with graphite paint and insulated by PVC foils of 100 μ m thickness. A strip board was pressed to the anode surface and the whole chamber was shielded with grounded planes.

5 Data on the gas mixtures

Following gas mixtures were tested in the RPC prototype:

- Ar 87% + iso-C₄H₁₀ 13% (referred as argon-isobutane)
- Ar 35% + iso-C₄H₁₀ 6% + CF₄ 59% (referred as argon-isobutane-freon)

The first mixture is a noble gas with small addition of a quenching gas - isobutane. The second mixture contains large amount of an electronegative gas - freon R-14 (CF₄) and similar ratio of argon to isobutane.

In order to simulate the electron avalanches with GARFIELD, a drift chamber simulation program (see Section 6), several gas properties must be provided: number of primary clusters per unit length and cluster size distributions, Townsend and attachment coefficients, longitudinal and transverse diffusion coefficients, electron drift velocity and positive ion mobility. When no experimental data were found some predictions obtained with gas simulation programs were used instead (MAGBOLTZ [15] in Section 5.4, HEED [16] in Section 5.2).

5.1 Specific primary ionisation

Specific primary ionisation (SPI) in gases in the minimum ionising region were taken from Ref [6, 7]. Measurements of SPI are difficult because high efficiency of single electron detection is required. For argon in particular results differ because usually a small fraction of quenching gas is added and SPI for pure argon is then extracted. One of the recent attempts of determining SPI may be found in Ref [7], where other results are discussed as well. For Ar and iso-C₄H₁₀ data obtained by Malamud et al. were used and for CF₄ those by Rieke and William. Both experiments used minimum ionising β -electrons. Table 2 summarises measurements of number of primary clusters per unit length.

Gas	Ref [7]		Ref [6]	
	SPI [cm ⁻¹ Torr ⁻¹]	Accuracy [%]	SPI [cm ⁻¹ Torr ⁻¹]	Accuracy [%]
Ar	0.029	≤15	0.030	0.7
iso-C ₄ H ₁₀	0.120	≤5	0.109	0.4
CF ₄	—	—	0.067	1.8

Table 2: Specific primary ionisation normalised to a temperature of 21° C. Data from Ref [6, 7].

For mixture of gases $G_1 \dots G_N$ the following formula was used [7]:

$$SPI_{\text{mix}} = \sum_{i=1}^N \frac{\pi_i}{\pi_1 + \dots + \pi_N} SPI(i)$$

where $SPI(i)$ denotes specific primary ionisation for G_i and π_i - atomic or molecular number multiplied by partial pressure of gas G_i in mixture.

5.2 Cluster size distribution

There are very few experiments in which number of electrons per cluster was measured. Recent work [8] by Fischle et al. reports on the cluster size (CS) distribution in argon and hydrocarbons. Fast β -electrons were used as ionising particles. The experimental results for argon differ from theoretical predictions by Lapique and Piuz [9]. No data were found for CF₄. Some Monte Carlo based programs, like HEED [16], allow to calculate the ionisation energy loss, number of

primary clusters per unit length and number of electrons per cluster in different materials. The measured and/or calculated cluster size distributions $w(n)$ for argon, methane, isobutane and CF_4 are shown in Figures 6, 7, 8, 9 respectively. In GARFIELD simulation experimental data were used for Ar and iso- C_4H_{10} together with the HEED predictions for freon. Most clusters (65÷80%) have size of $n = 1$. Table 3 shows probability $w(n)$ for $n = 1 \dots 5$.

Cluster size n	Probability $w(n)$ [%]					
	Ar			iso- C_4H_{10}		CF_4
	[8]	[9]	[16]	[8]	[16]	[16]
1	65.6	80.2	81.6	78.6	81.5	67.1
2	15.0	7.7	5.9	12.0	10.3	17.5
3	6.4	2.0	2.0	3.4	2.8	6.2
4	3.5	1.3	1.3	1.6	1.3	2.9
5	2.3	0.8	0.93	0.95	0.67	1.5

Table 3: Cluster size distributions in different gases. HEED [16] calculations for muons in minimum ionising region ($\gamma=4$). Lapique and Piuz [9] prediction for argon for minimum ionising particle ($\gamma=4$). Experimental data [8] for fast β -electrons ($\beta=0.8\div0.97$).

For mixture of gases $G_1 \dots G_N$ the following relation was used [8]:

$$w(n) = \sum_{i=1}^N \frac{\pi_i}{\pi_1 + \dots + \pi_N} w_i(n)$$

where $w_i(n)$ is the CS distribution for G_i and π_i is the partial pressure of G_i multiplied by the specific primary ionisation cross section (measured in [6]).

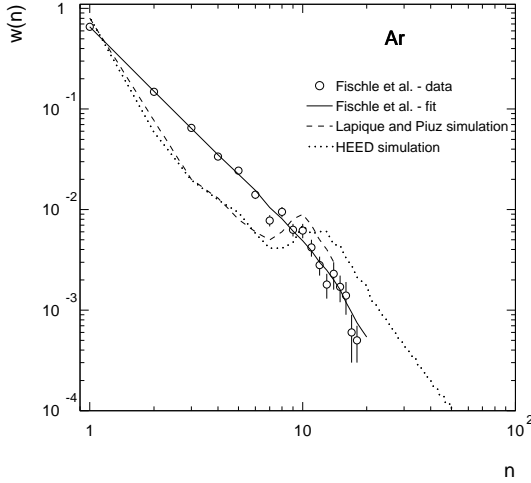


Figure 6: Cluster size distribution for argon. Experimental data [8] and simulations [9, 16].

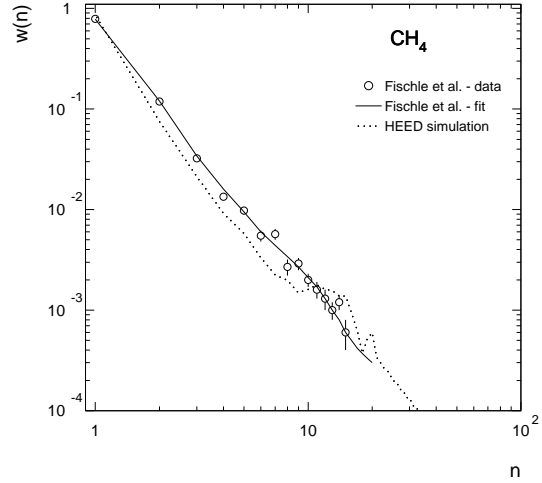


Figure 7: Cluster size distribution for methane. Experimental data [8] and HEED simulation [16].

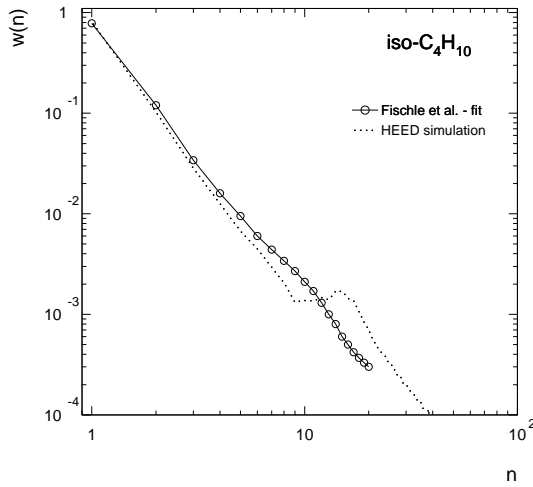


Figure 8: Cluster size distribution for isobutane. Fit valid for: CH_4 , C_2H_6 , C_3H_8 , $\text{iso-C}_4\text{H}_{10}$ [8] (solid line) and HEED simulation [16].

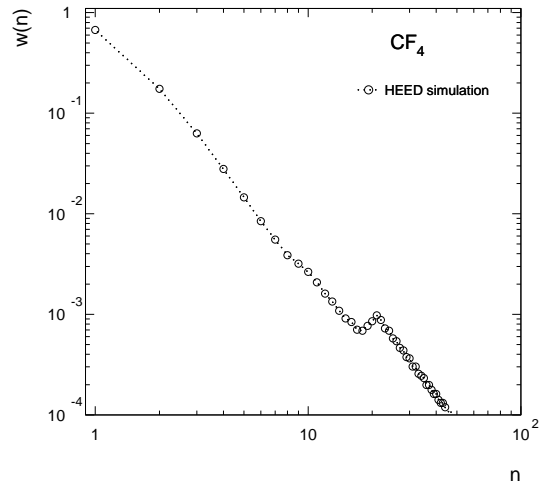


Figure 9: Cluster size distribution for freon CF_4 simulated with HEED [16].

5.3 Mobility of positive ions

Drift velocity of positive ions v_{drift}^+ linearly depends on the reduced field E/p up to very high field strengths, where it becomes proportional to $\sqrt{E/p}$. Thus the mobility, defined as $\mu^+ = v_{\text{drift}}^+/E$, can be treated as a constant for wide range of E at given p .

In mixture of gases $G_1 \dots G_N$ several kinds of positive ions are produced. The mobility $\mu(I^+)$ of ion I^+ is given by the Blanc's law [5]:

$$\frac{1}{\mu(I^+)} = \sum_{k=1}^N \frac{f(k)}{\mu(I^+, k)},$$

where $f(k)$ is a volume fraction of gas G_k in the mixture, $\mu(I^+, k)$ is the mobility of ion I^+ in gas G_k . However due to charge transfer with gas molecules all kinds of positive ions except one with the lowest ionisation potential are removed [10]. In mixture of hydrocarbons: methane, ethane, isobutane with Ar and/or CF_4 , hydrocarbons have lower ionisation potential (12.6 eV, 11.52 eV, 10.67 eV respectively) than argon (15.759 eV) and CF_4 (15.9 eV). Table 4 summarises measurements of positive ion mobilities found in the literature.

To compute ion mobility for gases under study, the measurements from Ref [5, 4, 10] were used and the Blanc's law applied. The migrating ions were assumed to be hydrocarbons. The calculated values were: $\mu^+ = 1.31 \text{ cm}^2\text{V}^{-1}\text{s}^{-1}$ for argon-isobutane and $\mu^+ = 1.01 \text{ cm}^2\text{V}^{-1}\text{s}^{-1}$ for argon-isobutane-freon.

Ion	Mobility [$\text{cm}^2\text{V}^{-1}\text{s}^{-1}$]		
	in Ar	in CF_4	in iso- C_4H_{10}
Ar^+	1.7	—	—
iso- $\text{C}_4\text{H}_{10}^+$	0.614	1.00	1.56

Table 4: Mobilities of positive ions. Data from Ref [5, 4, 10].

5.4 Gain, drift velocity and diffusion

There are few works [13, 14] in which the Townsend coefficient α/p was measured in commonly used gas mixtures for uniform field geometry at large electric fields, $E/p > 20 \text{ Vcm}^{-1}\text{Torr}^{-1}$. Many data exist for electron drift velocity and diffusion for various mixtures at low electric fields [11]. Unfortunately, the RPCs are operated at relatively high electric field strengths where no measurements are available. Therefore one has to either interpolate/extrapolate existing experimental data or calculate Townsend coefficient, diffusion and drift velocity for gas mixture from the first principles using cross section for electrons interacting with media and distribution of energy loss per collision. A MAGBOLTZ code [15] by S. Biagi allows one to calculate drift velocity, transverse and longitudinal diffusion coefficients, Townsend and attachment coefficients. The program contains the database of many gases (eg. Ar, CH₄, iso-C₄H₁₀, DME, CF₄), and solves the Boltzmann transport equation with addition of ionisation and attachment cross sections for requested mixture at a given E , p and T . The second order solution involves more detailed gas simulation and uses as an input the first order results.

Calculated drift velocity and diffusion agree with experimental data in low E/p region ($< 10 \text{ Vcm}^{-1}\text{Torr}^{-1}$). It was assumed that predictions are also valid for large values of E/p . However, calculated Townsend coefficient can easily disagree with existing data. Drift velocity and diffusion were calculated with MAGBOLTZ. First and second order solutions can be seen on Figure 10. Difference between two steps is a rough estimation of accuracy of the result. It is significant only for argon-isobutane-freon mixture ($< 7\%$). Longitudinal (along vector of electric field strength) and transverse diffusion coefficients are plotted on Figure 11 (second order solutions). They were normalised to 1 cm of drift with a constant electric field, namely $\sigma = \sqrt{2D} \text{ 1cm}/v_{\text{drift}}$ where D is the "real" diffusion coefficient (in units cm^2s^{-1}). The longitudinal diffusion which mostly affects drift time of electrons to anode plane is smaller than transverse one. It can be also seen that argon-isobutane-freon mixture has lower diffusion coefficients. For argon-isobutane mixture α/p was calculated using the formula:

$$\alpha/p (E/p) = A \exp(-Bp/E)$$

where parameters A and B depend only on the fraction of a quencher component (isobutane). In Ref [13] parameters A and B were obtained as a fit to experimental data for several quencher fractions and results are reproduced in Table 5.

Composition		A	B	Remarks
Ar	iso-C ₄ H ₁₀	[cm ⁻¹ Torr ⁻¹]	[Vcm ⁻¹ Torr ⁻¹]	
91.79 %	8.21 %	22.45	127.6	data, valid for $E/p < 20.1 \text{ Vcm}^{-1}\text{Torr}^{-1}$
87 %	13 %	39.37	150.6	interpolation
79.3 %	20.7 %	70.70	193.2	data, valid for $E/p < 25.5 \text{ Vcm}^{-1}\text{Torr}^{-1}$

Table 5: Measured and interpolated parameters A and B used in formula $\alpha/p = A \exp(-B p/E)$ for argon-isobutane mixtures. Data from Ref [13].

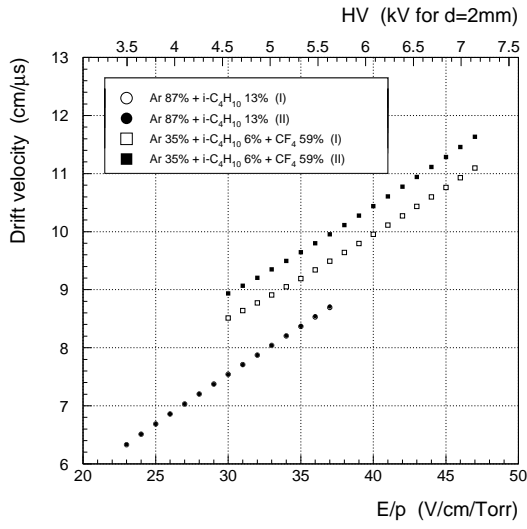


Figure 10: Electron drift velocity vs E/p calculated with MAGBOLTZ for argon-isobutane and argon-isobutane-freon mixtures (first and second order solutions, for argon-isobutane differences are very small).

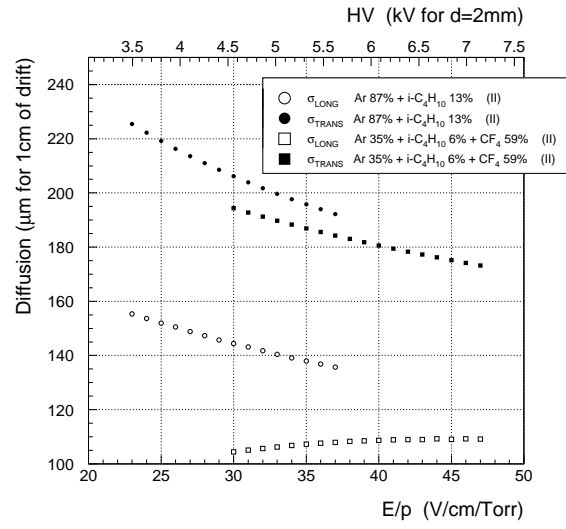


Figure 11: Longitudinal (empty points) and transverse (filled points) diffusion coefficients for 1 cm of drift with constant electric field vs E/p obtained with MAGBOLTZ for argon-isobutane and argon-isobutane-freon mixtures. (second order solutions).

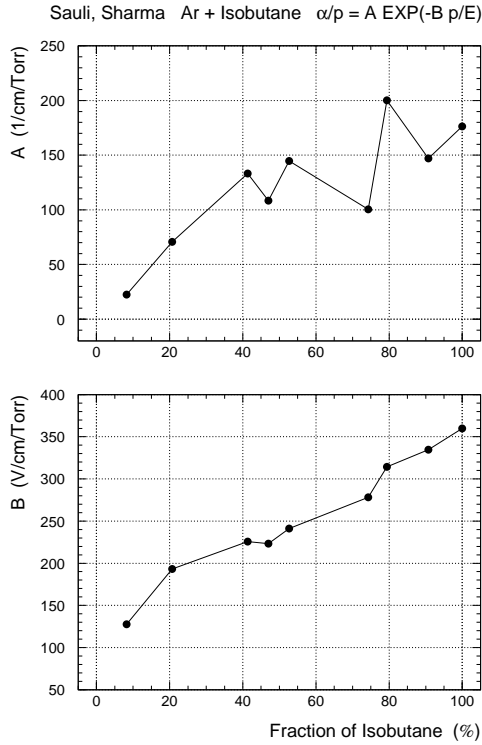


Figure 12: Dependence of parameters A and B on isobutane concentration in Ar + iso- C_4H_{10} mixture. Data from Ref [13].

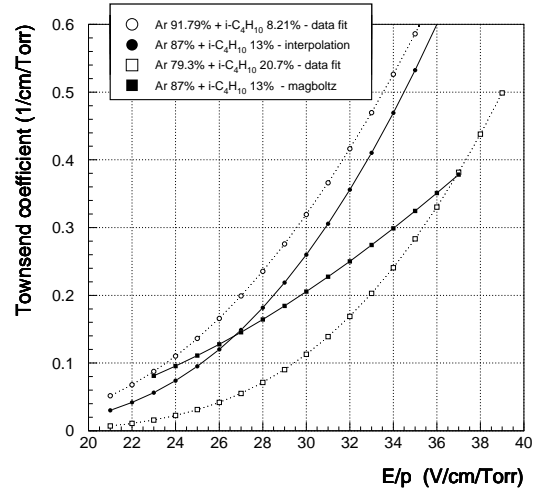


Figure 13: Comparison of Townsend coefficients obtained by interpolation of experimental data (full circles) and by MAGBOLTZ calculation (full squares) for Ar 87% + iso- C_4H_{10} 13%. Fit to exp. data (dotted lines) from Ref [13].

Figure 12 shows A and B as a function of isobutane fraction.

For tested argon-isobutane mixture parameters A and B were interpolated. It was assumed that parametrisations from Ref [13] are also valid in the experimentally studied region $E/p = 23 \div 30 \text{ Vcm}^{-1}\text{Torr}^{-1}$. The result can be seen on Figure 13. The Townsend coefficient obtained with MAGBOLTZ is also shown. It can be seen that curves corresponding to experimental data have different slopes than MAGBOLTZ prediction. The losses due to attachment could be neglected since calculated ratio of attachment to Townsend coefficient was of order of $10^{-2} \div 10^{-3}$.

For argon-isobutane-freon mixture the Townsend and attachment coefficients were calculated with MAGBOLTZ (experimentally studied region $E/p = 43 \div 47 \text{ Vcm}^{-1}\text{Torr}^{-1}$). In this case losses due to attachment were significant as can be seen from Figure 14. For this mixture the reduced electric field necessary to achieve the same gas gain was greater by $17 \div 19 \text{ Vcm}^{-1}\text{Torr}^{-1}$ (accordingly, by $2.6 \text{ kV} \div 2.9 \text{ kV}$ for 2 mm gap RPC), see Figure 15.

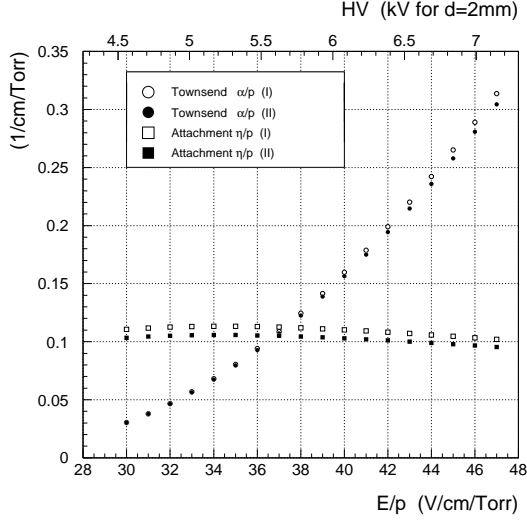


Figure 14: Townsend and attachment coefficients vs E/p calculated with MAGBOLTZ for Ar 35%+iso- C_4H_{10} 6%+ CF_4 59% (first and second order solutions).

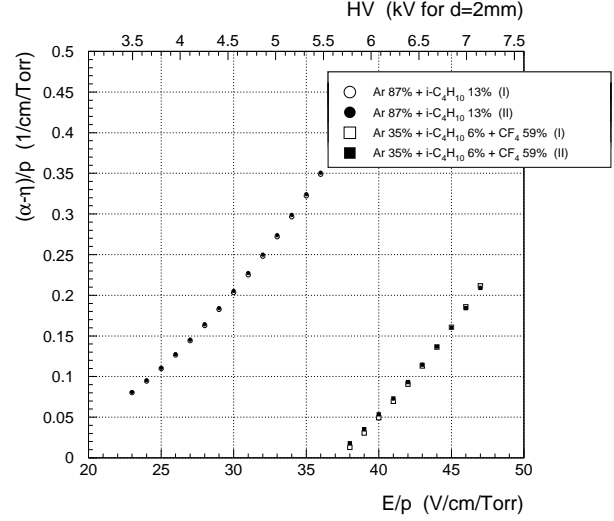


Figure 15: Effective Townsend coefficient (with attachment losses) vs E/p calculated with MAGBOLTZ for argon-isobutane and argon-isobutane-freon mixtures (first and second order solutions).

6 Simulation with GARFIELD

GARFIELD, a drift-chamber simulation program [12] has been adopted to simulate discharges in the RPC gas gap. The features of the program are the following:

- 2-dimensional electric field geometry, defined by planes (and wires) at constant potentials
- setting arbitrary gas properties: drift velocity, ion mobility, transverse and longitudinal diffusion, Townsend and attachment coefficient, cluster formation
- defining 2-dimensional particle track, calculating electron and ion drift lines (in 3 dimensions), generating electron avalanches.

It was assumed that the chamber was operated at atmospheric pressure $p=760$ Torr and at room temperature $T=20^\circ$ C.

6.1 Geometry

In order to simulate current $I(t)$ flowing across the gas gap of the thickness d a following model was used. Two parallel electrodes (anode at potential $V=0$, cathode at $V = -U_o$), formed an uniform electric field $E_o = U_o/d$. A minimum ionising particle crossed a gas volume at instant $t = 0$ at zenith angle θ . Figure 16 shows an example of generated clusters along particle track and calculated electron drift lines. Two cases were investigated:

- $\theta = 0^\circ$
- θ followed angular distribution of cosmic rays for $\theta < 30^\circ$.

Chamber of gap thickness $d=2$ mm was considered.

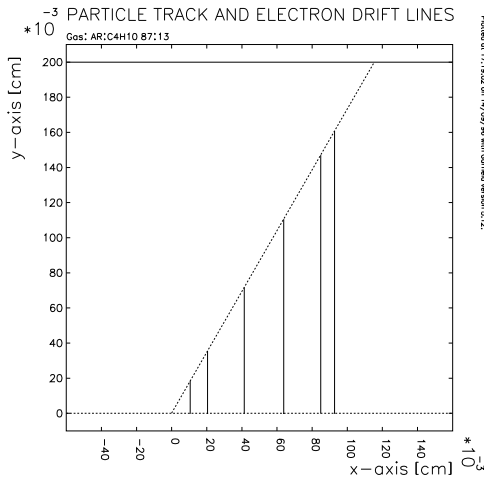


Figure 16: GARFIELD example of an event in which 6 primary ionisations took place (14 electron-ion pairs were created). Electron drift lines to anode are shown. Particle entered the gas gap at zenith angle 30° .

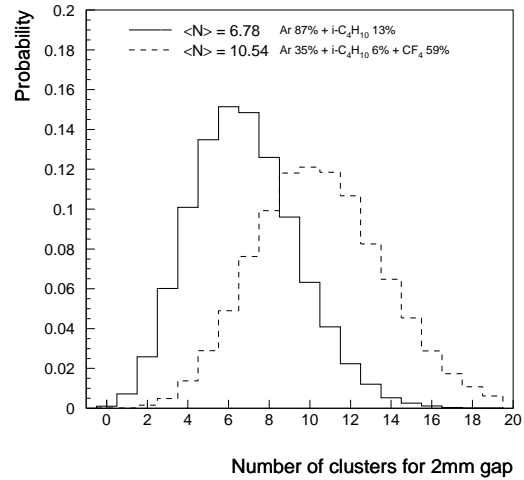


Figure 17: Number of generated clusters for 2 mm gap in argon-isobutane and argon-isobutane-freon mixtures.

6.2 Description of the model

For each set of gas and electric field sample of 4000 events was simulated. The U_o range corresponded to that studied experimentally (Section 9), namely, $U_o = 3.5 \div 4.6$ kV for argon-isobutane and $U_o = 6 \div 7.1$ kV for argon-isobutane-freon mixture.

The number of primary ionisation events per unit length is Poisson distributed with an average \bar{n} . The distance between two clusters, Δx , is independent of the position of other clusters and it is exponentially distributed

$$f(\Delta x) = \bar{n} \exp(-\bar{n} \Delta x).$$

The distance x of the j -th cluster (first cluster is closest to cathode) from the begin of the track on cathode plane follows distribution

$$A_j(x) = \frac{x^{j-1}}{(j-1)!} \bar{n}^j \exp(-\bar{n} x).$$

For argon-isobutane $\bar{n} = 34.02$ pairs/cm was taken and for argon-isobutane-freon $\bar{n} = 52.75$ pairs/cm. Distributions of number of generated clusters in single event are compared in Figure 17 for two gases studied. Since \bar{n} is greater for argon-isobutane-freon mixture the average distance between two clusters is smaller as can be seen from Figures 18 and 19. The minimal inefficiency for 2 mm gap (no clusters generated in gas volume) amounts to $\varepsilon_{\text{ineff}} = \exp(-\bar{n}d)$ and is equal to 0.111% for argon-isobutane and 0.003% for argon-isobutane-freon.

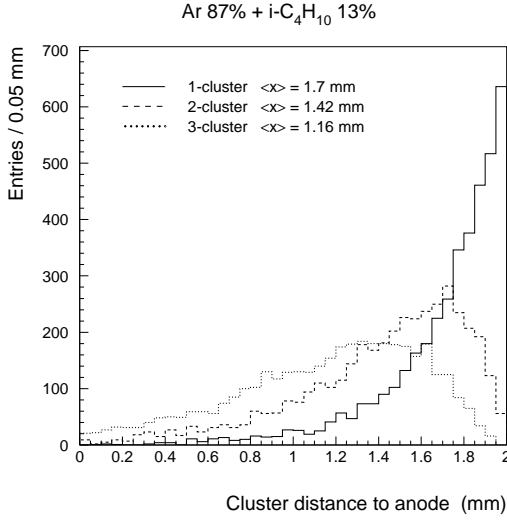


Figure 18: Distribution of the distance of j -th cluster to anode (1-st cluster is closest to cathode) for argon-isobutane.

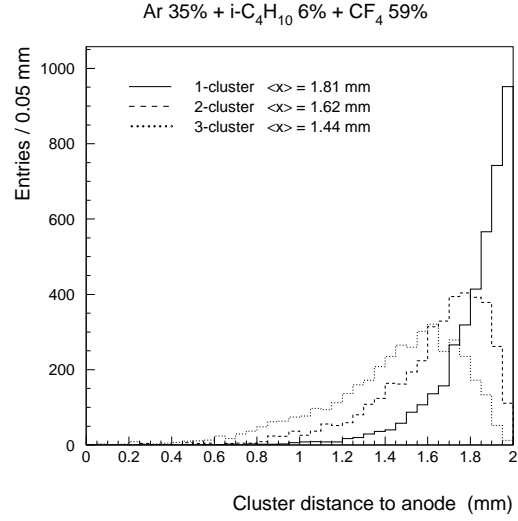


Figure 19: Same as Figure 18 for argon-isobutane-freon.

Number of primary electrons in each cluster was generated from given previously calculated CS distribution. Cluster sizes up to 100 electrons were considered. Mean numbers of electrons created in a single cluster were similar for two gas mixtures, namely: 2.096 for argon-isobutane and 2.112 for argon-isobutane-freon.

From each generated cluster electron drift line was calculated. Then the drift time to anode t_o , the integrated multiplication factor M_o and integrated diffusion σ were computed. It was assumed that each electron-ion pair started a single avalanche.

The arrival time was drawn from normal distribution with mean t_o and dispersion σ , where

$$\sigma = \int_{\text{drift-line}} \frac{\sigma_{\text{diff}}(z)^2}{v_{\text{drift}}(z)^2} dz.$$

The final diffusion σ_{diff} was extracted from transverse and longitudinal diffusion coefficients.

The multiplication factor of the avalanche is subjected to statistical fluctuations. If $M_o = \exp(\alpha x)$ is the mean electron number after covering the distance x the probability of having gain M , in case of $M_o \gg 1$, is equal to

$$p(M, x) = \frac{1}{M_o} e^{-M/M_o}.$$

6.3 Electron and ion currents

A modification to GARFIELD has been made to allow calculation of electric current in gas gap, later used as an input to the SPICE electronics circuitry simulation program. For signal developing it was assumed that ionisation act took place at $t = 0$ and n_o primary electron-ion pairs were created at distance d_o from cathode (see Figure 20). Those pairs started an avalanche, whose gain was determined by the Townsend coefficient α . Drift velocities of charge carriers were assumed to be constant during the whole time of signal formation (effect of diffusion was taken into account by means of fluctuations in electron drift velocity according to fluctuations in electron drift time to anode).

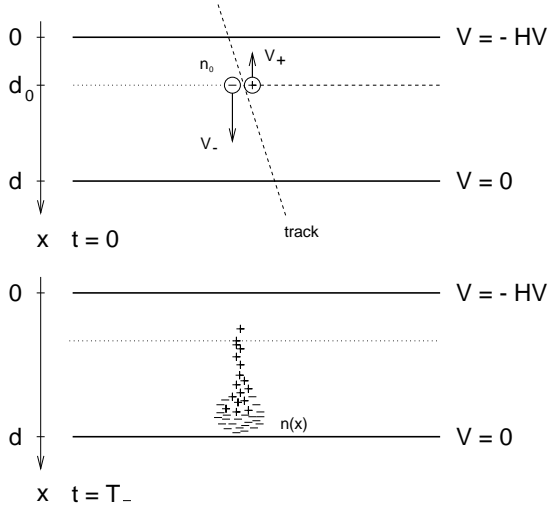


Figure 20: Electron-ion pair created at d_o from cathode, starting avalanche at instant $t = 0$.

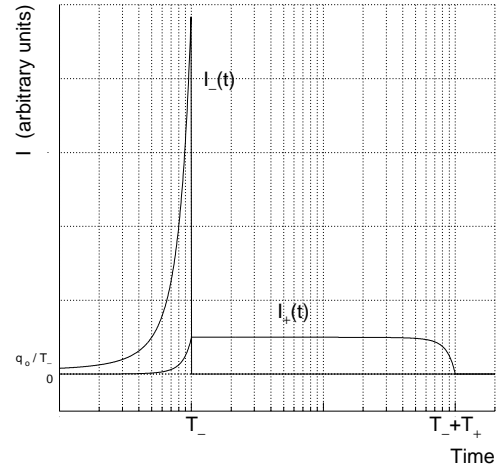


Figure 21: Shapes of the currents I_- and I_+ in case of $T_+ = 100T_-$.

Since drift velocity of electrons, v_- , is $100 \div 1000$ times larger than that of ions, v_+ , electrons need time of order of tens nanoseconds to cross the gap, while ions need few microseconds.

The signal $I(t)$ in the external circuit consists of two components:

- $I_-(t)$ - "fast" electron component, due to drift of electrons to anode
- $I_+(t)$ - "slow" ion tail, due to movement of positive ions to cathode.

Following the arguments presented in Ref [17] (and neglecting secondary effects such as photo-effect) after solving the Townsend equations one obtains:

$$I_-(t) = \begin{cases} \frac{q_o v_-}{d} \exp[\alpha v_- t] & t \leq T_- \\ 0 & t > T_- \end{cases}$$

$$I_+(t) = \begin{cases} \frac{q_o}{T_+} \left\{ \exp[\alpha v_- t] - \exp\left[\alpha v \left(t - \frac{d_o}{v_+}\right) \theta\left(t - \frac{d_o}{v_+}\right)\right] \right\} & t \leq T_- \\ \frac{q_o}{T_+} \left\{ \exp[\alpha(d - d_o)] - \exp\left[\alpha v \left(t - \frac{d_o}{v_+}\right) \theta\left(t - \frac{d_o}{v_+}\right)\right] \right\} & T_- < t \leq T_- + T_+ \end{cases}$$

where

$$\begin{aligned}
T_- &= \frac{d-d_0}{v_-} && \text{drift time of electrons to anode} \\
T_+ &= \frac{d}{v_+} && \text{drift time of positive ions to cathode} \\
q_0 &&& \text{primary charge} \\
\theta(x) &&& \text{unit step function} \\
\text{and} \quad \frac{1}{v} &= \frac{1}{v_-} + \frac{1}{v_+}.
\end{aligned}$$

Figure 21 shows relation between I_- and I_+ , when $T_+ \approx 100 T_-$. When attachment plays role additional current of negative ions $I_n(t)$ formed from electron capture by gas molecules should be added as well. In above formulae α has to be replaced by effective Townsend coefficient $\alpha_{\text{eff}} = \alpha - \eta$ and $I_+(t)$ multiplied by factor $\alpha/(\alpha - \eta)$. Since $v_+ \ll v_-$ (and the drift speed of negative ions $v_n \approx v_+$) currents $I_+(t)$ and $I_n(t)$ can be neglected for $t < T_-$.

The total signal is the sum of all signals from single electron avalanches ($q_0 = e_0$).

6.4 Total and visible charges

After integrating fast electron component one obtains the "visible" charge

$$Q_{\text{vis}} = \frac{Q_{\text{tot}} - q_0}{\alpha d} \approx_{q_0 \ll Q_{\text{tot}}} \frac{Q_{\text{tot}}}{\alpha d}, \text{ where total charge } Q_{\text{tot}} = q_0 \exp[\alpha(d - d_0)].$$

For instance six clusters in event shown in Figure 16 generated the current in external circuit shown in Figure 22 (electron component) and in Figure 23 (ion tail). In this case $Q_{\text{vis}} \approx 6\% \cdot Q_{\text{tot}}$.

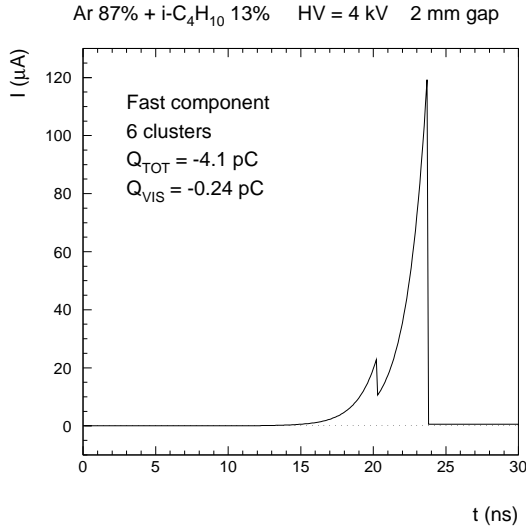


Figure 22: Fast electron component of the current induced in event shown in Figure 16.

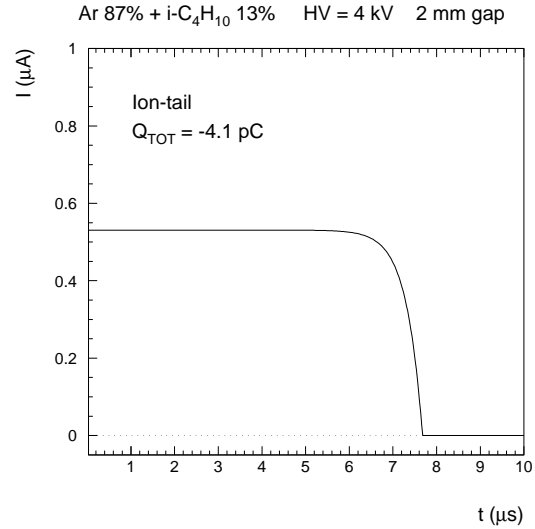


Figure 23: Slow positive ion component of the current induced in event shown in Figure 16.

When gain increases the ratio of visible to total charge decreases as $1/\alpha$. This is illustrated in Figure 24 for two gas mixtures considered. In the studied U_0 region this ratio changed from 20% to 3%.

On the average contribution of the j -th cluster to the visible charge can be expressed as

$$R_j = \frac{k^j}{k + k^2 + \dots + k^{j_{\text{max}}}}$$

where $k \equiv \exp(-\alpha \Delta x)$ and Δx denotes mean distance between two clusters. Thus R_1 grows with α to 1 and R_j decreases to zero after reaching a maximal value for $j \geq 2$. Comparison between two gases is shown in Figure 25.

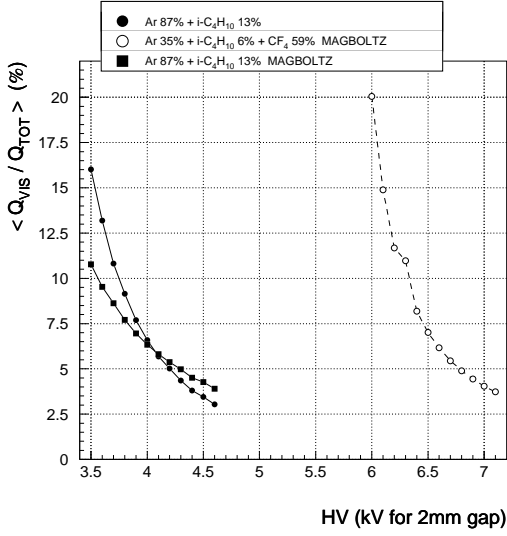


Figure 24: Mean ratio of Q_{vis} to Q_{tot} vs the high voltage for two gases studied.

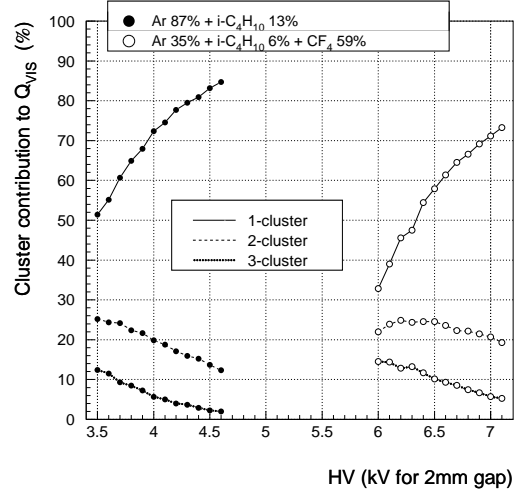


Figure 25: Contribution of the j -th cluster visible charge to Q_{vis} (1-st cluster is closest to cathode).

6.5 Gain and streamer probability

In an uniform electric field, E_0 , the Townsend mechanism of avalanche growth, $M = \exp(\alpha x)$, is no longer valid when electrical field due to space charge of electrons and ions, E_r , cannot be neglected with respect to the applied field E_0 . The electric field is increased in front of the electron cloud and behind positive ions cloud, while it is reduced inside the avalanche volume.

The field distortion by $\sim 1\%$ may occur at $\sim 10^6$ gain. The avalanches with higher multiplication factor ($M > 5 \cdot 10^6 \div 10^7$) become less frequent as a result of the reduction of effective α in the Townsend formula due to positive ions charge [17].

In addition at higher amplification factors $\sim 10^7 \div 10^9$ very rapid plasma streamers occur which lead to breakdown. The condition for critical avalanche size, by Rather, roughly assumes that breakdown takes place when $E_r \cong E_0$ or $\alpha x_{\text{crit}} \cong 20$. The streamer probability depends on x/x_{crit} and increases with cluster size (since each electron starts single avalanche). Even when $x/x_{\text{crit}} < 1$ breakdown may occur because of gain fluctuations.

Some quantitative models exist [18] which reproduce experimentally observed breakdown threshold in certain gas mixtures.

In this analysis it was assumed that:

- Townsend mechanism was also valid at higher gains
- streamer occurred when at least one avalanche had size that exceeded critical value (integrated Townsend coefficient $\alpha x > 20$).

Those events which did not fulfill the streamer condition were referred as events in avalanche mode.

An example of gains obtained for avalanches started by single electrons is plotted in Figure 26 for argon-isobutane at $U_0=4$ kV. The dashed line indicates critical gain and the white one mean gain M_0 as a function of drift length x . Some of the avalanches reached breakdown limit although their $x/x_{\text{crit}} < 1$.

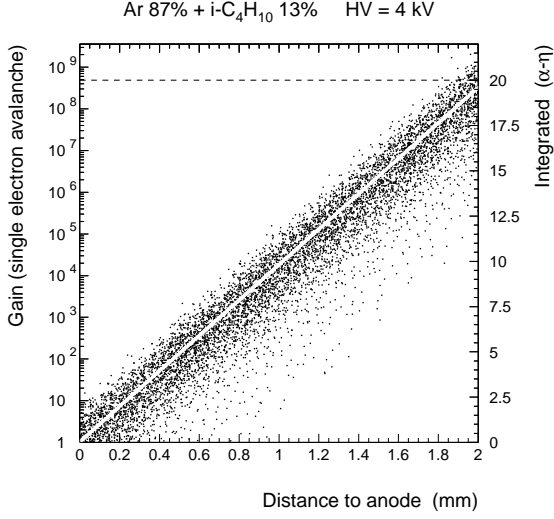


Figure 26: Gain of avalanches started by single electron as a function of drift length (argon-isobutane mixture at HV=4 kV). White line shows dependence of mean multiplication factor on drift length. Dashed line denotes breakdown threshold.

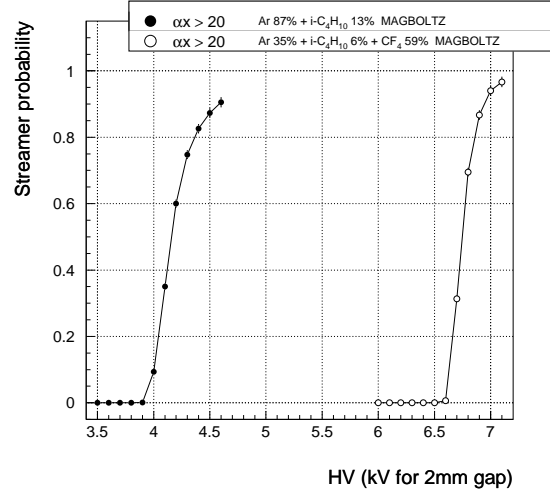


Figure 27: Streamer probability vs the high voltage for two gas mixtures (streamer condition: $\alpha x > 20$).

Ar 87% + iso-C ₄ H ₁₀ 13%				
2 mm gap HV [kV]	MAGBOLTZ		Interpolation	
	$\langle Q_{\text{vis}} \rangle$ aval. mode [pC]	Streamer prob. [%]	$\langle Q_{\text{vis}} \rangle$ aval. mode [pC]	Streamer prob. [%]
3.5	$3.9 \cdot 10^{-3}$	0	$2.0 \cdot 10^{-4}$	0
3.6	$1.2 \cdot 10^{-2}$	0	$7.2 \cdot 10^{-4}$	0
3.7	$4.3 \cdot 10^{-2}$	0	$3.7 \cdot 10^{-3}$	0
3.8	0.177	0	$2.1 \cdot 10^{-2}$	0
3.9	0.79	0.1	0.186	0
4.0	2.71	9.4	1.66	2.9
4.1	4.37	35	4.53	42
4.2	4.30	60	3.99	73
4.3	4.43	75	3.19	86
4.4	3.82	83	3.54	93
4.5	4.06	87	2.46	95
4.6	4.18	91	2.09	97

Table 6: Mean visible charge (in avalanche mode) and streamer probability (streamer condition: $\alpha x > 20$) predicted for argon-isobutane. Results compared for α/p calculated with MAGBOLTZ and interpolated from measurements [13].

Ar 35% + iso-C ₄ H ₁₀ 6% + CF ₄ 59%		
2 mm gap HV [kV]	MAGBOLTZ	
	$\langle Q_{\text{vis}} \rangle$	Streamer
	aval. mode [pC]	prob. [%]
6.0	$7.83 \cdot 10^{-5}$	0
6.1	$2.77 \cdot 10^{-4}$	0
6.2	$1.24 \cdot 10^{-3}$	0
6.3	$4.83 \cdot 10^{-3}$	0
6.4	$3.60 \cdot 10^{-2}$	0
6.5	0.23	0
6.6	1.61	0.6
6.7	5.75	31
6.8	8.74	69
6.9	8.77	87
7.0	6.74	94
7.1	6.22	97

Table 7: Mean visible charge (in avalanche mode) and streamer probability (streamer condition: $\alpha x > 20$) predicted for argon-isobutane-freon. Parameters η/p , α/p calculated with MAGBOLTZ.

The streamer probability was defined as the fraction of events that fulfill streamer condition: $\alpha x > 20$. Its dependence on the high voltage is shown in Figure 27 for two gas mixtures. The streamer mode dominated for argon-isobutane when $U_o > 4.1$ kV and for argon-isobutane-freon mixture when $U_o > 6.7$ kV. The numeric values are also shown in Tables 6 and 7. It should be noted that the transition between low- and high streamer probability regions happens after change of only 200 V and the difference of $2.6 \div 2.7$ kV is predicted for transition point between chamber filled with argon-isobutane and with argon-isobutane-freon.

6.6 Charge spectra

Obtained charge spectra may be overestimated at higher gains since space-charge effect was not taken into account. An example of Q_{vis} distributions (normalised to 1) for argon-isobutane at low gain ($U_o = 3.8$ kV, without streamers) and at high gain ($U_o = 4.1$ kV, with streamers) can be seen in Figures 28 and 29, respectively. In the second case, the contribution of events that probably caused breakdown (according to the assumed model) was shown as a dashed area.

For each U_o value only events in avalanche mode were selected and their mean charge was calculated. The resulting Q_{vis} distributions are plotted in Figure 30 for argon-isobutane and in Figure 31 for argon-isobutane-freon mixtures.

Finally, the mean visible charge of events in avalanche mode can be seen in Figure 32. The numerical values are shown in Tables 6 and 7. A decrease of $\langle Q_{\text{vis}} \rangle$ with the high voltage occurred. This can be explained by dividing the gas gap into streamer region (in which avalanches have drift length $x > x_{\text{crit}}$) and avalanche region ($x < x_{\text{crit}}$). As effective α increases with the applied field x_{crit} becomes smaller and the streamer region grows. Hence the mean distance from anode of clusters generated in non-streamer region is lower, and therefore the mean charge decreases as well.

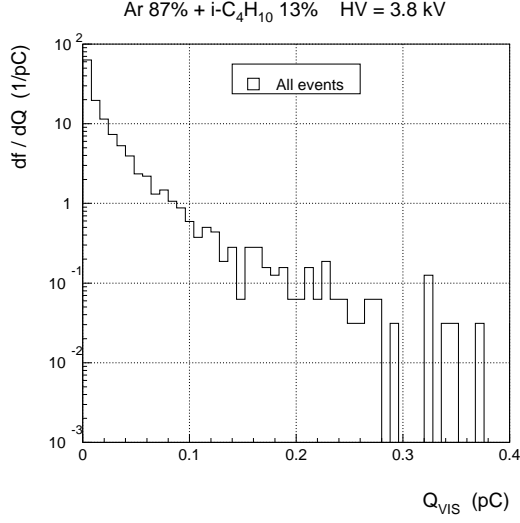


Figure 28: Visible charge distribution for argon-isobutane at HV=3.8 kV.

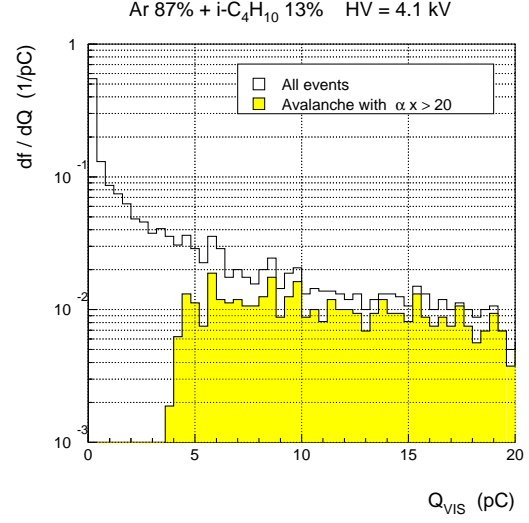


Figure 29: Visible charge distribution for argon-isobutane at HV=4.1 kV. Contribution of events that met streamer condition $\alpha x > 20$ is shown (dashed area).

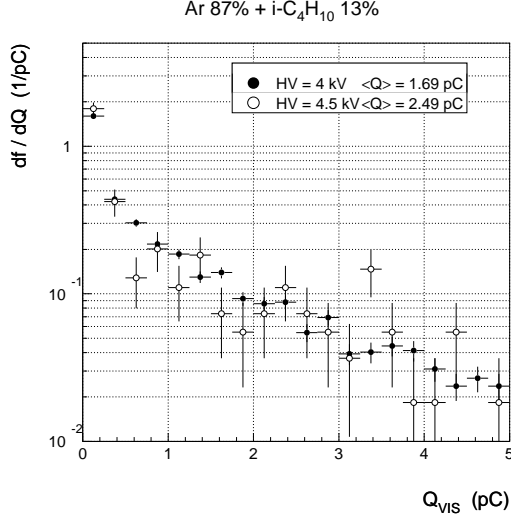


Figure 30: Q_{vis} distributions of events in avalanche mode for two HV sets for argon-isobutane mixture.

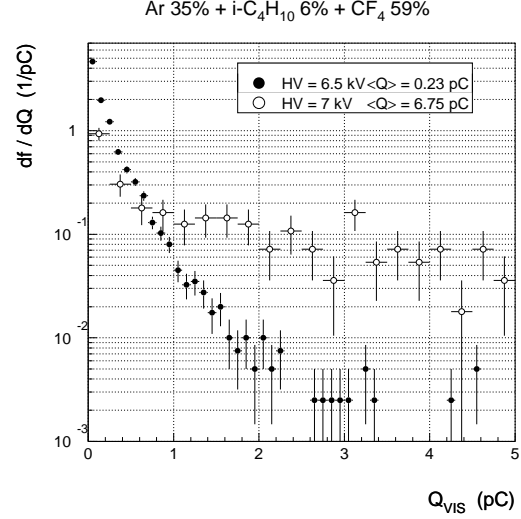


Figure 31: Q_{vis} distributions of events in avalanche mode for two HV sets for argon-isobutane-freon mixture.

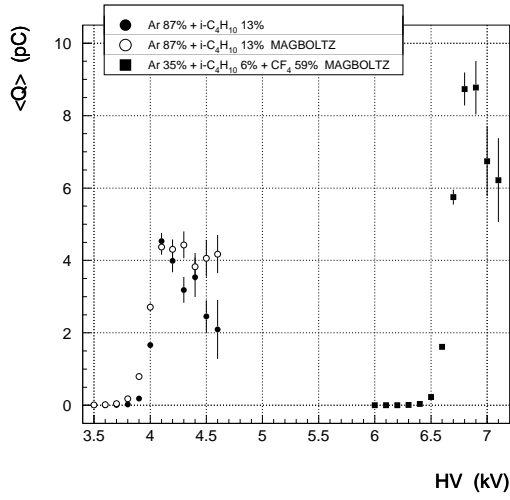


Figure 32: Mean visible charges of events in avalanche mode vs the high voltage for two simulated gases.

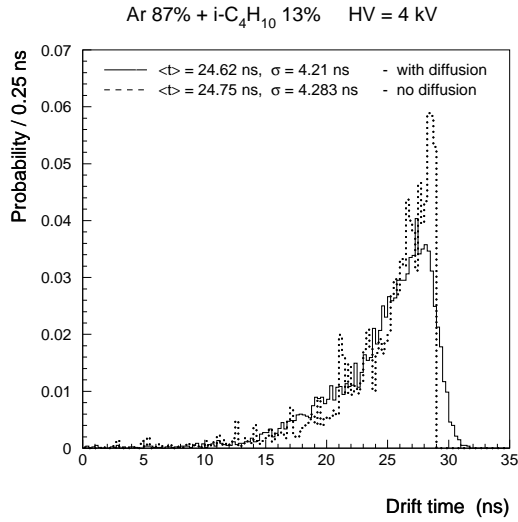


Figure 33: Drift times of electrons from 1-st cluster (closest to cathode) with and without diffusion.

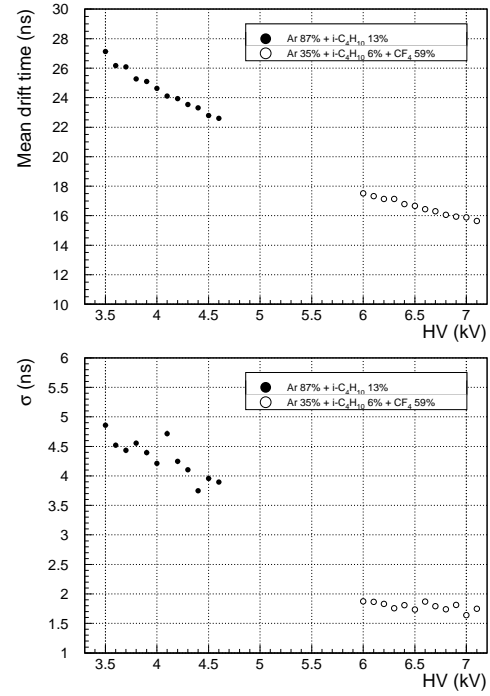


Figure 34: Mean drift time and dispersion of electrons from 1-st cluster (closest to cathode) as a function of the high voltage for two gases studied .

6.7 Timing and effect of diffusion

Simulations with and without diffusion were performed for argon-isobutane at $U_o=4$ kV. When diffusion was neglected, all pairs which originated from the same cluster had identical drift time. Pairs origing from the first cluster (closest to cathode), which mainly contributed to the electron signal, had greater integrated diffusion. Arrival time distributions of those pairs with and without effect of diffusion can be compared from Figure 33. When diffusion was taken into account the spread in time was greater by about 0.07 ns.

In reality, space charge field ($E_r > 1\% \cdot E_o$) may alter electron velocity and electron cloud size may exceed the effect of diffusion [18].

Because electron drift velocity rises with E/p the mean drift time to anode (and dispersion) drops with the high voltage. The mean and dispersion of arrival time for pairs from the first cluster are compared in Figure 34 for two gas mixtures. For argon-isobutane-freon signals rise faster with smaller dispersion in the studied HV region.

However, for signals induced on strips, σ is smaller because only pulses that passed the discrimination threshold are detected. This prediction on σ can be treated as the worse case of detector resolution.

6.8 Effect of varying gap thickness

In order to take into account some mechanical inaccuracies which might occur during chamber assembly and/or operation a variation by 0.1 mm from 2 mm gap was simulated for argon-isobutane mixture at $U_o=4$ kV. The resulting change of the applied field by $\pm 5\%$ (equivalent to $\Delta U_o = \pm 200$ V) lead to significant changes in amplification factor and streamer probability. The results are shown in Table 8.

Ar 87% + iso-C ₄ H ₁₀ 13% $U_o = 4$ kV		
Gap thickness [mm]	$\langle Q_{vis} \rangle$ aval. mode [pC]	Streamer prob. [%]
1.9	3.84	65
2	1.66	2.9
2.1	$5.0 \cdot 10^{-2}$	0

Table 8: Mean visible charge (in avalanche mode) and streamer probability (streamer condition: $\alpha x > 20$) for three gap thickness ($U_o = 4$ kV). Parameter α/p interpolated from measurements [13].

6.9 Effect of varying gas composition

Small changes of a quencher fraction may lead to strong variations in avalanche gain. For Ar 87% + iso-C₄H₁₀ 13% mixture at $U_o = 4$ kV variation in gas composition by 1% were considered. Differences are remarkable as can be seen from data in Table 9.

Ar % + iso-C ₄ H ₁₀ % $U_o = 4$ kV		
iso-C ₄ H ₁₀ fraction [%]	$\langle Q_{\text{vis}} \rangle$ aval. mode [pC]	Streamer prob. [%]
12	3.68	28
13	1.66	2.9
14	0.37	0

Table 9: Mean visible charge (in avalanche mode) and streamer probability (streamer condition: $\alpha x > 20$) for small variations in isobutane concentration ($U_o = 4$ kV, 2 mm gap). Parameter α/p interpolated from measurements [13].

6.10 Effect of varying SPI

Because number of primary ionisation clusters was not precisely known the effect of changing SPI by $\pm 20\%$ were taken into account. Simulation was performed for argon-isobutane at $U_o = 4$ kV. The mean visible charge in the avalanche mode changed from nominal $\langle Q_{\text{vis}} \rangle = 1.67$ pC to 1.31 pC (-20% SPI) and 2.07 pC ($+20\%$ SPI).

6.11 Effect of varying incident track angle θ

Cosmic rays of $\theta < 30^\circ$ for argon-isobutane at $U_o = 4$ kV were simulated. When track was not perpendicular to the chamber's plane more ionisation clusters were expected along the track. In this case the mean visible charge (events in avalanche mode) increased by about 23% ($\langle Q_{\text{vis}} \rangle = 2.05$ pC).

7 RPC working model

In order to investigate development of signals induced on strips two working models were tested using SPICE, an analog circuitry simulation program. The chamber was divided into elementary cells, each represented by resistors and capacitors. In addition one cell contained the current source (signals simulated with GARFIELD for argon-isobutane at HV=4 kV for 2 mm gap RPC).

Because strips were 1 cm wide cells had area of 1 cm² in the first model (discharge in gas volume of 1 cm × 1 cm × 2mm). In total 5×5 cells were simulated with 5 read-out strips (covered area 5×5 cm²). Each cell consisted of (Figures 35 and 36):

- capacitance of gas volume, $C_{\text{gas}} = \epsilon_0 \frac{S}{d} = 0.443 \text{ pF}$, where: $S=1 \text{ cm}^2$, $d=2 \text{ mm}$ (estimate)
- capacitance of melamine plate, $C_{\text{bulk}} = \epsilon_0 \epsilon \frac{S}{d} = 4.43 \text{ pF}$, where: $\epsilon=5$, $S=1 \text{ cm}^2$, $d=1 \text{ mm}$ (estimate)
- resistance of melamine plate, $R_{\text{bulk}} = \rho \frac{d}{S} = 10^{11} \Omega$, where: $\rho = 10^{12} \Omega \cdot \text{cm}$, $S=1 \text{ cm}^2$, $d=1 \text{ mm}$ (estimate)
- resistance R_{surf} , the surface resistivity of melamine layer, assumed to be same as R_{bulk}
- resistance $R_{\text{grap}} = \sigma \frac{l}{a} = 10 \text{ k}\Omega$, where: $\sigma \approx 10 \text{ k}\Omega/\square$ – measured surface resistivity of the graphite layer, $l=1 \text{ cm}$ – the distance between central points of two adjacent cells, $a=1 \text{ cm}$ – the cell width
- capacitance of HV graphite layer to the grounded plane, $C_{\text{up}} = 1.5 \text{ pF}$ (measurement)
- capacitance of GND graphite layer to the strip surface, $C_{\text{down}} = 10 \text{ pF}$ (measurement).

Each cell was connected to the appropriate strip as schematically shown in Figure 37. The strip was represented as:

- capacitance (area 1 cm×22 cm) to grounded plane, $C_0 = 50 \text{ pF}$ (measurement)
- load resistance of read-out electronics, $R_0 = 50 \Omega$.

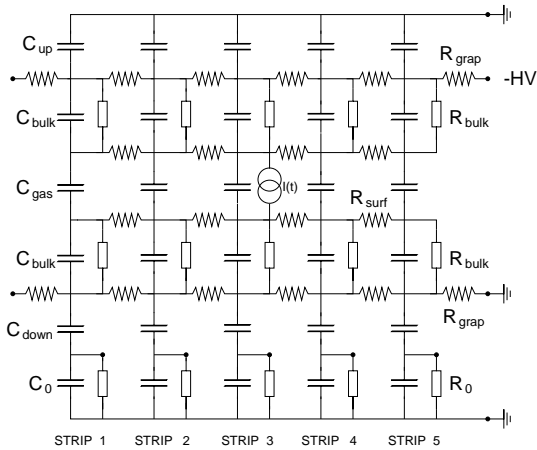


Figure 35: A model with 5×5 cells and 5 read-out strips (front view).

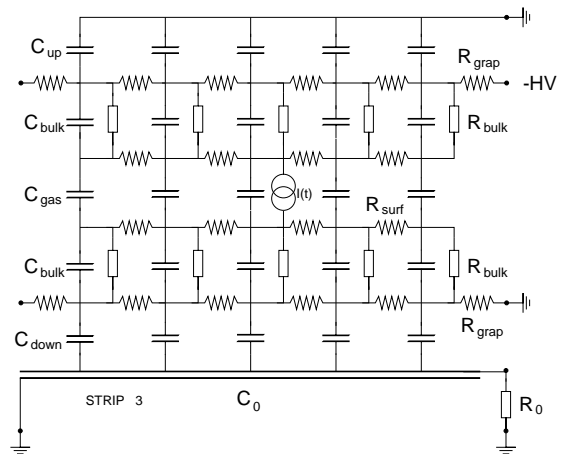
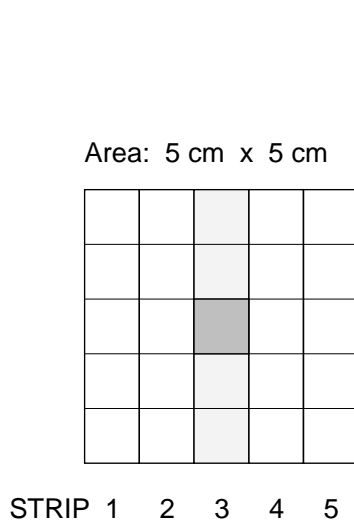
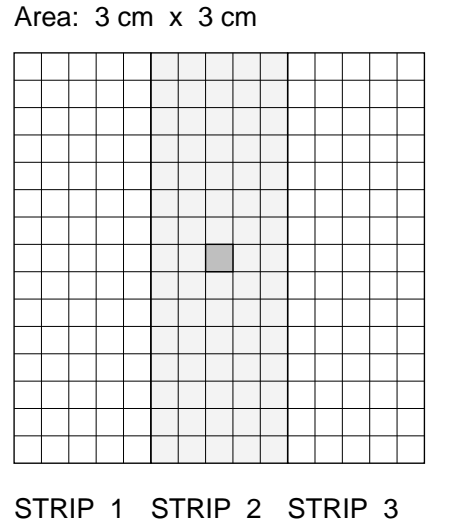


Figure 36: A model with 5×5 cells and 5 read-out strips (side view).



- cell with current source
- cells connected to central strip

Figure 37: A model with 5×5 cells and 5 read-out strips covered area of $5 \times 5 \text{ cm}^2$ (top view).



- cell with current source
- cells connected to central strip

Figure 38: A model with 15×15 cells and 3 read-out strips covered area of $3 \times 3 \text{ cm}^2$ (top view).

In the second model 15×15 cells were simulated, each of $2 \times 2 \text{ mm}^2$ area (25 cells/cm^2 , 3 read-out strips, covered area $3 \times 3 \text{ cm}^2$). A schematic view can be seen in Figure 38.

7.1 Single cell

Let us consider single cell during discharge and assume no current dissipation on the graphite layer and neglect finite bulk and surface resistivities of electrodes ($R_{\text{grap}}, R_{\text{bulk}}, R_{\text{surf}} \rightarrow +\infty$). The equivalent circuit is shown in Figure 39. For a gas current compound $I(t)$ of frequency f ($\omega = 2\pi f$):

- strip impedance is equal to $Z_0 = \frac{R_0}{1 + i\omega R_0 C_0}$
- impedances of capacitors $C_{\text{gas}}, C_{\text{bulk}}, C_{\text{up}}, C_{\text{down}}$ are equal accordingly to $Z_{\text{gas}}, Z_{\text{bulk}}, Z_{\text{up}}, Z_{\text{down}}$, where $Z = \frac{1}{i\omega C}$.

The read-out electronics measure current I_0 flowing through resistor R_0 . Therefore

$$\begin{cases} I_0 = \frac{Z_{\text{gas}}}{Z_{\text{gas}} + 2Z_{\text{bulk}} + Z_{\text{up}} + Z_{\text{down}} + Z_0} \frac{Z_0}{R_0} I \\ U_0 = I_0 R_0 . \end{cases}$$

For the detection purpose one is particularly interested in maximal signal amplitude I_0^{max} (or U_0^{max}) and collected charge $Q_0 = \int_0^T I_0(t) dt$. The maximal current decreases with frequency f and its upper limit is given by

$$|I_0| = [1 + C_{\text{gas}}(2C_{\text{bulk}}^{-1} + C_{\text{up}}^{-1} + C_{\text{down}}^{-1})] |I| \approx 0.65 |I| .$$

The characteristic time constant of the pulse rise is $\tau = 1/\alpha v_- \sim 2 \text{ ns}$ which corresponds to frequency of 500 MHz (eg. $\alpha/p = 0.12 \text{ cm}^{-1} \text{ Torr}^{-1}$, $v_- = 7 \text{ cm}/\mu\text{s}$).

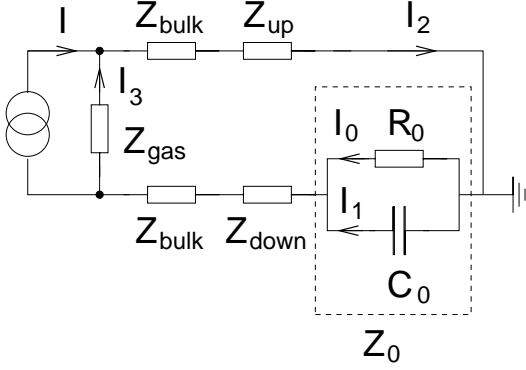


Figure 39: Circuit for a single cell. Surface resistivity of melamine and graphite layers were neglected.

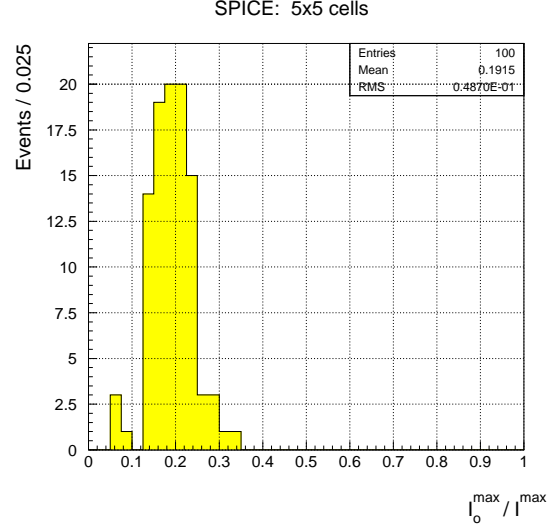


Figure 40: Ratio of the peak current flowing through the load resistance R_0 and the peak current flowing across the gas gap.

7.2 Results on 5×5 cells model

100 signals obtained with GARFIELD were processed using 5×5 cells model and different values of C_0 and σ ($C_0 = 50$ pF, 100 pF, $\sigma = 10$, 100 k Ω/\square).

The peak current I_0^{\max} measured on strip was about 10-20% of the maximal current in the gas I^{\max} . Current shapes of I and I_0 in a typical event are shown in Figure 42. The distribution of I_0^{\max}/I^{\max} ratio can be seen in Figure 40 ($C_0 = 50$ pF, $\sigma = 10$ k Ω/\square). The mean value increased with decreasing strip capacitance C_0 and was equal to 13% for $C_0 = 100$ pF and 19% for $C_0 = 50$ pF.

The integrated charge from strip signals Q_{meas} was smaller than visible charge from fast electron component Q_{vis} by about factor of 2. This can be seen from Figure 43 ($C_0 = 50$ pF, $\sigma = 10$ k Ω/\square). The mean ratio was 62-65% for integrated charges over 100 ns time window. After imposing cut on signal amplitude, U_{thr} , this ratio dropped to 40-50%. Obtained $\langle Q_{\text{meas}}/Q_{\text{vis}} \rangle$ values for different cuts are listed in Table 10.

Cut	SPICE 100 evts.		Experiment 1000 evts.		
	$\langle Q_{\text{meas}}/Q_{\text{vis}} \rangle$	Efficiency		Efficiency	
U_{thr}^- [mV]	$\langle Q_{\text{meas}}/Q_{\text{vis}} \rangle$ [%]	$C_0 = 50 \text{ pF}$ [%]	$C_0 = 100 \text{ pF}$ [%]	Avalanche mode [%]	Total [%]
No cut	62–65	100	100	–	–
–0.8	45–48	64	58	55	65–70
–1	42–47	59–61	53–56	45	55–60
–2	38–45	50–51	44–45	25	35–40

Table 10: $\langle Q_{\text{meas}}/Q_{\text{vis}} \rangle$ and efficiency ($C_0 = 50$ pF, 100 pF, $\sigma = 10$, 100 k Ω/\square) from SPICE simulation and efficiency from experimental measurements for several cuts on signal amplitude (argon-isobutane at HV=4 kV).

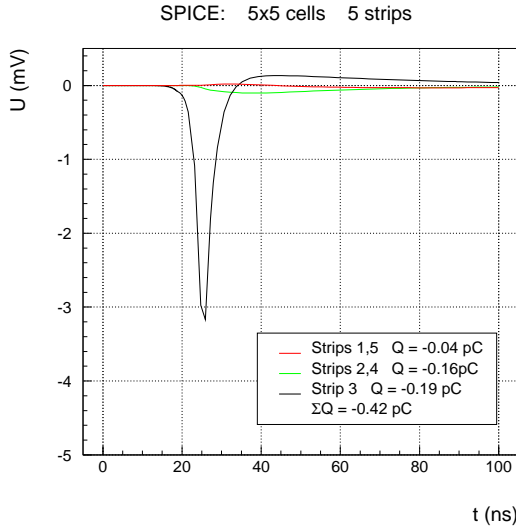


Figure 41: Strip signals obtained with 5×5 cells model with 5 read-out strips. Charges integrated over 100 ns time window.

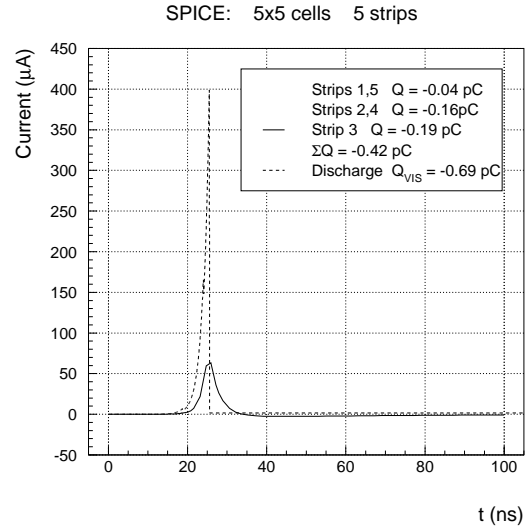


Figure 42: Current flowing across the gas gap (dashed line) and current flowing through the load resistance R_0 of pick-up strip (solid line). Visible charge of fast component and charges from integration of strip signals over 100 ns time window are shown. (5×5 cells model, 5 read-out strips)

Fraction of events that passed U_{thr}^- threshold is the simulated detector efficiency. In Section 9.8 experimental results on efficiency are presented. In Table 10 the measured and simulated efficiencies are shown for comparison (argon-isobutane at HV=4 kV). The total experimental efficiency (in the avalanche and streamer mode) is comparable with simulated ones, but statistic is rather small⁷.

For a given U_{thr}^- cut arrival time, time resolution and width of the signals were also studied. Arrival time distribution and signal width are plotted in Figures 45 and 46 respectively for $U_{\text{thr}}^- = -1$ mV ($C_0 = 50$ pF, $\sigma = 10$ kΩ/□). Depending on C_0 and σ parameters and U_{thr}^- cut simulated mean arrival time was 22–24 ns and time resolution was 1.5–1.9 ns. In relation to Figure 34 the mean arrival time increased and better time resolution was noticed.

The pulse width mainly depended on capacitance C_0 , namely 7–9 ns for $C_0 = 50$ pF and 9–14 ns for $C_0 = 100$ pF. Similar values were measured for pulses in avalanche mode (Section 9.4).

7.3 Results on 15×15 cells model

In order to investigate dependence of signal amplitude on position of the discharge in the chamber a 15×15 cells model was used. Only three read-out strips were simulated, because of the limited number of components in the SPICE simulator. The cell with current source, connected to central strip, was placed at three different positions: 1 mm (close to strip border), 3 mm and 5 mm (central position, see Figure 38). Long computing time prevented us from repeating the calculations for all 100 signals, as in the case of 5×5 model. Examples of signal shapes for various positions of the cell are shown in Figures 47, 48 and 49. In the first plot, two strips passed $U_{\text{thr}}^- = -1$ mV cut. It can be also seen that signal on strip 1 arrived after signal on strip 2 (which was closest to the discharge cell). The signal from the third plot can be compared to the

⁷Only 100 events were simulated with SPICE (for various C_0 and σ) because of long computing time. Small area of the detection system caused low rate of cosmic ray events ($\sim 10^{-2}$ Hz), thus only 1000 events were collected for each set of gas and HV (experimental setup in Section 8).

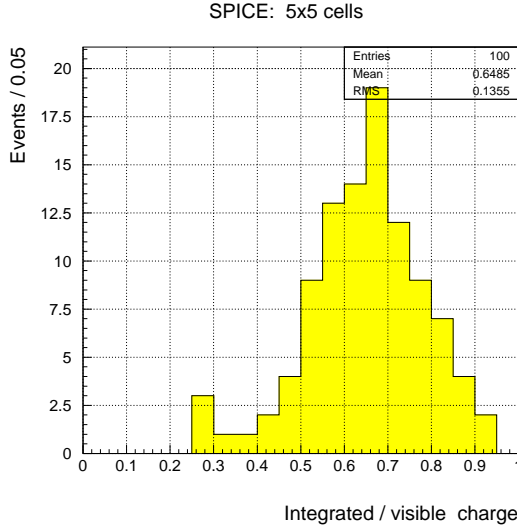


Figure 43: Ratio of integrated charge from all strips and visible charge of the fast electron component (5×5 cells model, 5 read-out strips, charges integrated over 100 ns time window).

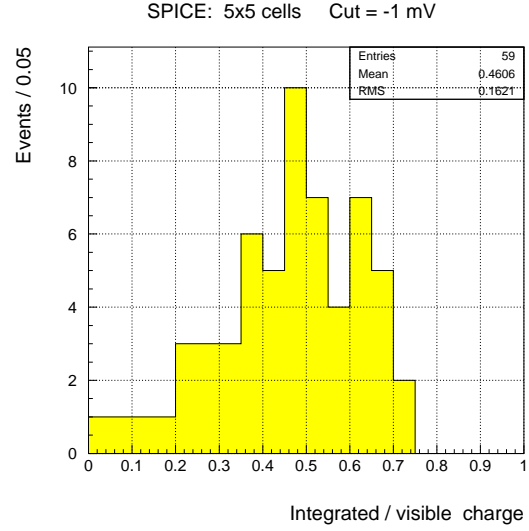


Figure 44: Ratio of integrated charge after $U_{\text{thr}}^- = -1$ mV cut and visible charge of the fast electron component (5×5 cells model, 5 read-out strips).

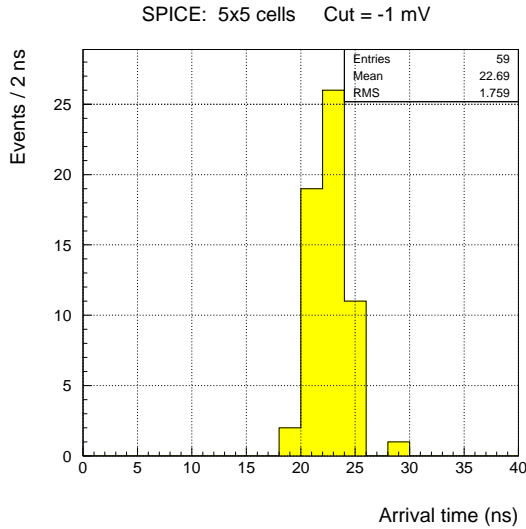


Figure 45: Arrival time of central strip signals for $U_{\text{thr}}^- = -1$ mV. (5×5 cells model, 5 read-out strips).

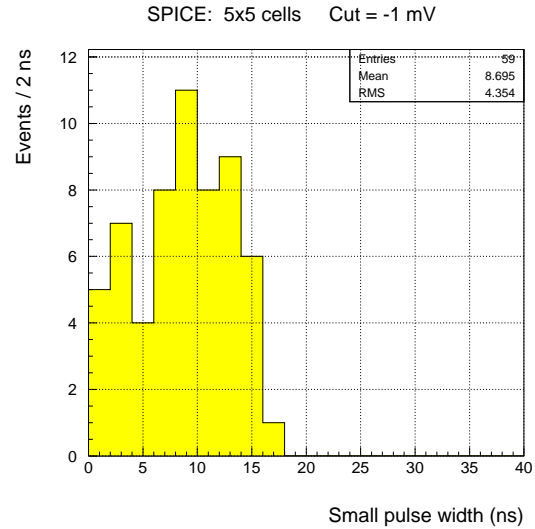


Figure 46: Width of central strip signals for $U_{\text{thr}}^- = -1$ mV. (5×5 cells model, 5 read-out strips).

prediction of 5×5 model shown in Figure 41 for the same event. In some of events differences of 1 mV can be noticed between two models.

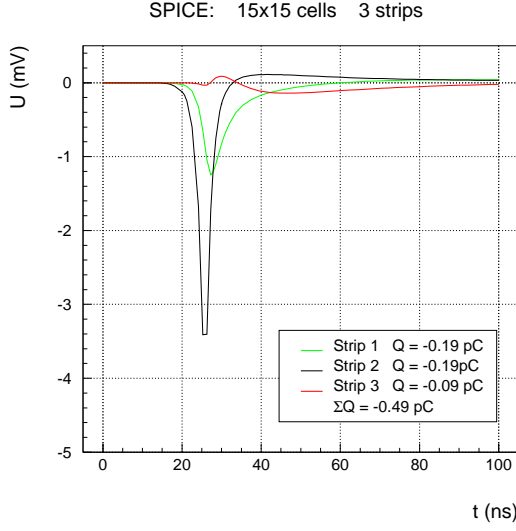


Figure 47: Strip signals obtained with 15×15 cells model with 3 read-out strips. Discharge cell located at 1 mm from the border of central strip. Charges integrated over 100 ns time window.

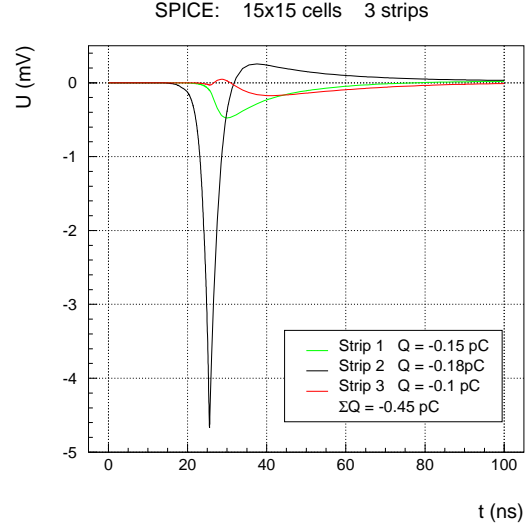


Figure 48: Strip signals obtained with 15×15 cells model with 3 read-out strips. Discharge cell located at 3 mm from the border of central strip. Charges integrated over 100 ns time window.

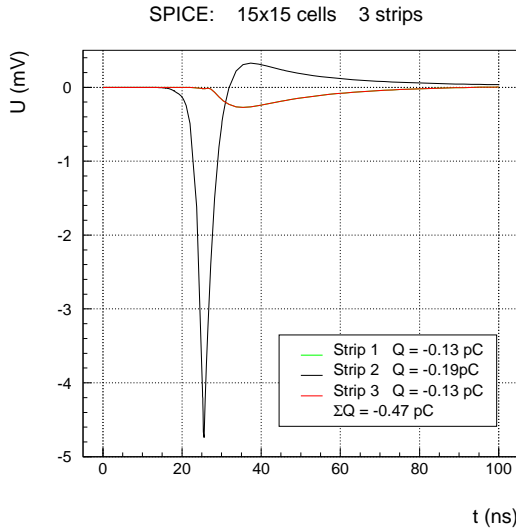


Figure 49: Strip signals obtained with 15×15 cells model with 3 read-out strips. Discharge cell located at 5 mm from the border of central strip (central position). Charges integrated over 100 ns time window.

8 Experimental setup

8.1 Geometry and triggering system

The RPC prototype was tested with cosmic rays. The chamber was externally triggered by two scintillators of $3.5 \times 10 \text{ cm}^2$ area. They were positioned at the centre of the chamber and at a distance of 18 cm from each other as shown in Figure 50. The zenith angles of incident particles did not exceed 30° . Analog signals from photo-multipliers were discriminated at -30 mV threshold and sent to a coincidence unit with gate shaper (250 ns width). A total rate of cosmic ray events was about 1 event per minute.

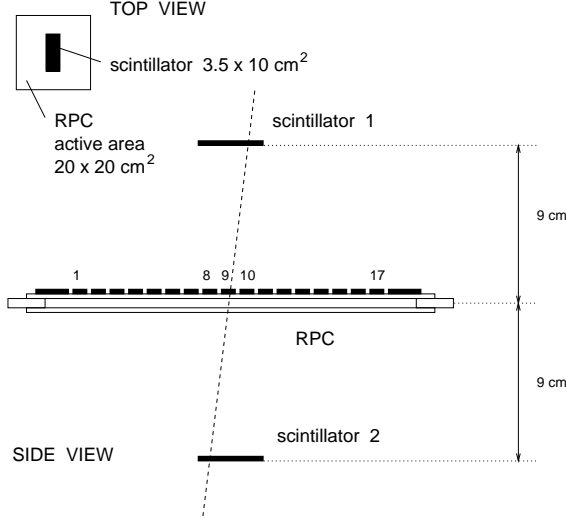


Figure 50: Experiment geometrical setup.

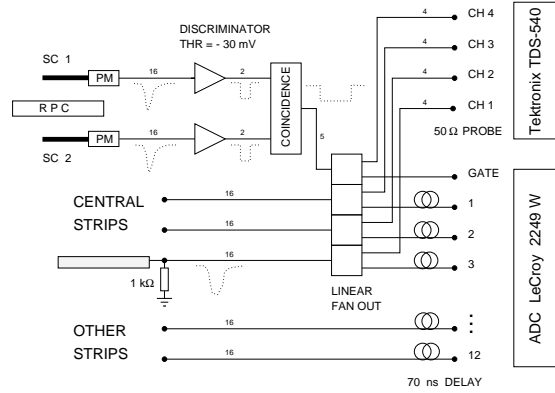


Figure 51: Experiment read-out scheme for ADC and digitising oscilloscope.

8.2 Read-out electronics

A scheme of electronic read-out is shown in Figure 51. To collect charges a copper strip board pressed to the RPC surface was used. Each strip of $1 \text{ cm} \times 22 \text{ cm}$ area was connected to ground through $1 \text{ k}\Omega$ resistance and via 50Ω LEMO cable to read-out electronics. Therefore 95% of induced charge was measured. Twelve strips (number 3÷14) were connected to LeCroy 2249W ADC module (1 count = 0.25 pC , 12-bits per channel). Signals from three central strips (number 8,9,10) were read-out with 4-channel Tektronix TDS-540 digitising oscilloscope with 50Ω probe. A fourth channel was connected to the coincidence unit and was used to trigger the scope (gate signal). Using a linear 4-channel FAN OUT unit the signals could be split to allow ADC and scope analysis at the same time. Time delay between gate and strip signals with and without FAN OUT remained the same.

Each channel was stored in the scope memory as 1000, 2500 or 5000 points with 20 ns/div (0.4 ns/point) or 50 ns/div (1 ns/point) time scales. However, with 4 channels being read-out simultaneously the real sampling rate was 250 MHz (4 ns/point) and amplitude of intermediate points was linearly interpolated. Full scale of amplitude corresponded to 256 counts (8 bits per channel), and several amplification scales were used: 1 mV/div (1 count= 0.04 mV), 2 mV/div (1 count= 0.08 mV), 5 mV/div (1 count= 0.2 mV) and 100 mV/div (1 count= 4 mV).

The scope was triggered when the negative slope of NIM gate signal reached -100 mV threshold (time instant $t=0$). When trigger was detected four channels stored in scope memory were sent to a PC-machine through GPIB card and saved for off-line analysis.

In general the gate signal arrived after signal from the strips. This delay was caused by propagation of the scintillator signal in photo-multiplier tube, discriminator, coincidence unit and cables. Additional measurements with scope showed that:

- dispersion between two photo-multiplier signals at -30 mV threshold was 2 ns
- overall estimated delay (including cables) between arrival time of analog signal to discriminator and trigger (measured at -100 mV threshold) was 45 ns with 1.8 ns dispersion

The last value does not take into account the propagation time of a signal in photo-tube which is typically 20 ns for this type of photo-multipliers.

9 Experimental results

The aim of this study is to investigate chamber response in the avalanche mode. In the following sections results on: timing, amplitude, charge, strip multiplicity and efficiency are discussed.

The following gas mixtures were tested:

- Ar 87% + iso-C₄H₁₀ 13% (referred as argon-isobutane mixture)
- Ar 86% + iso-C₄H₁₀ 12% + CF₄ 2%
- Ar 78% + iso-C₄H₁₀ 11% + CF₄ 11%
- Ar 35% + iso-C₄H₁₀ 6% + CF₄ 59% (referred as argon-isobutane-freon mixture)

All gases used were commercially available versions and no special treatment was applied to achieve high gas purity (eg. to eliminate water and oxygen contaminations). The high voltage, pressure, temperature and flow meters were not constantly monitored, either.

For each set of gas and high voltage a sample of about 1000 cosmic ray events was collected (run).

9.1 Event classification

An off-line analysis program was developed to recognise small pulses (in avalanche mode) and big pulses (in streamer mode). Therefore events can be classified into four groups (classes):

- only small pulse
- big with small pulse (in this case small pulse is called precursor)
- only big pulse
- empty event.

9.1.1 Small pulse

A small pulse is characterised by relatively small charge (below few pC) and amplitude (few mV) and short time duration (below 30 ns). Figure 52 gives an example of small pulse. Several quantities can be studied, namely: arrival time with respect to the gate, width, amplitude and charge. To obtain the charge two methods were used: integrating a signal over pulse width and integrating over constant time window.

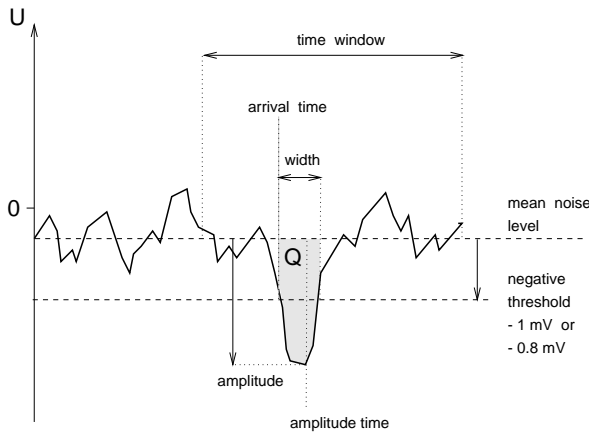


Figure 52: Variables used for small pulse analysis.

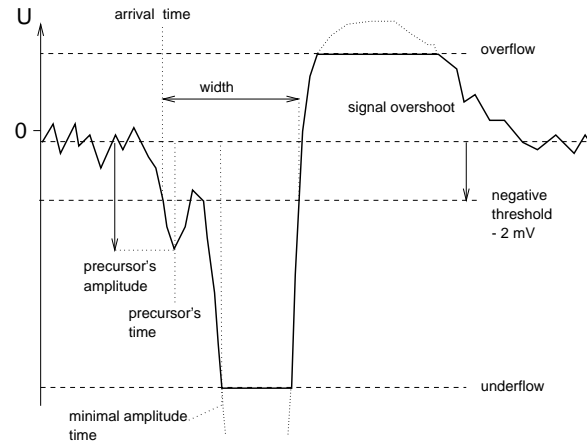


Figure 53: Variables used for big pulse analysis.

In every event mean noise level was calculated from the first few hundred points for each channel. A small pulse was detected if its amplitude reached negative threshold (with respect to the calculated mean noise level) within given time window (100 ns before gate). Selecting of U_{thr}^- should be taken with care, because too high threshold increases probability of detecting noise fluctuation instead of good signal, while too low one causes loss in efficiency.

An example of noise amplitude spectrum of a single run is given in Figure 54 and mean $|U_{\text{noise}}|$ for all runs is plotted in Figure 55. The noise amplitude varied between channels and between runs, and in most cases $|U_{\text{noise}}|$ did not exceed 1 mV and its mean value was about 0.15 mV. The analysis was performed using cuts: $U_{\text{thr}}^- = -0.8$ mV, -1 mV and -2 mV⁸. To minimise possibility of detecting large noise fluctuations (oscillation-like) an additional cut was imposed, namely, that the noise amplitude must not exceed positive threshold of $U_{\text{thr}}^+ = 1.5$ mV within time window.

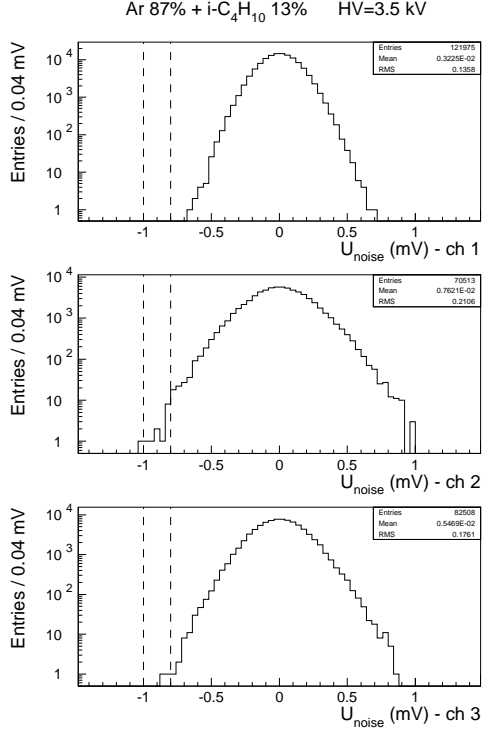


Figure 54: Noise amplitude spectra in a typical run (dashed lines indicate used cuts).

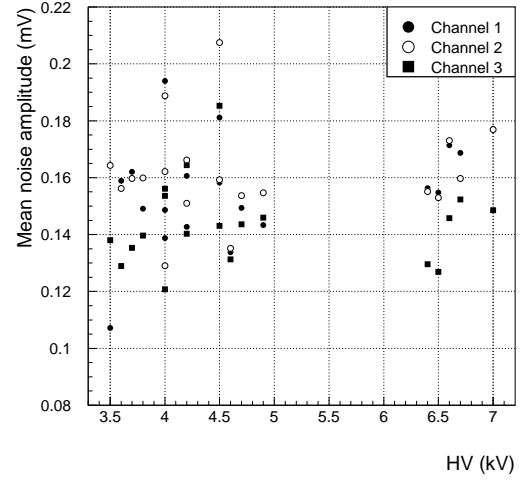


Figure 55: Mean (absolute) noise amplitudes for all runs.

Small pulses were detected independently for three channels and the signal which arrived first was called main small pulse. (in most cases it has the maximal amplitude). An example of event with two small pulses can be seen in Figure 56 (time scale in nanoseconds, voltage scale in millivolts).

⁸It is possible to set threshold individually for each run depending on maximal noise amplitude fluctuations, but these cuts were used consequently to make comparison between runs easier.

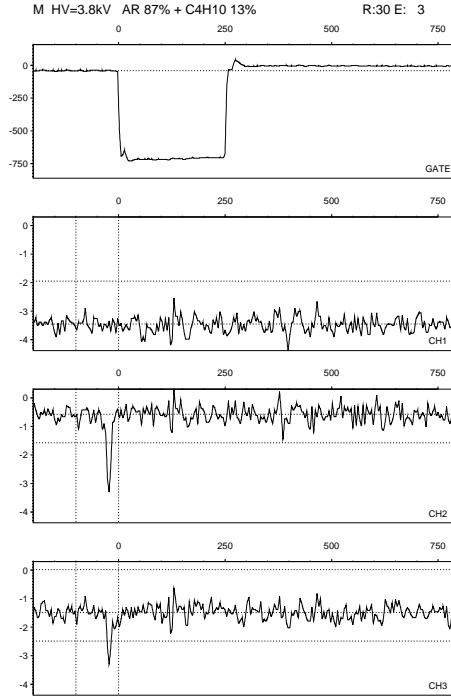


Figure 56: Event with two small pulses with integrated charges: -0.5 pC, -0.3 pC. Dotted lines indicate mean noise level, positive and negative cuts and time window. Upper signal is the scope trigger, while three lower signals correspond to strips 8,9,10 (1 mV/div).

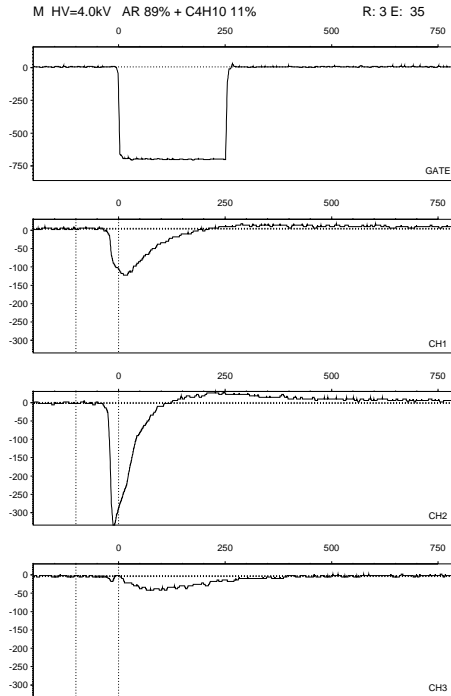


Figure 57: Typical big discharge. Main big pulse on channel 2. Integrated charges: -168 pC, -170 pC, -145 pC (100 mV/div).

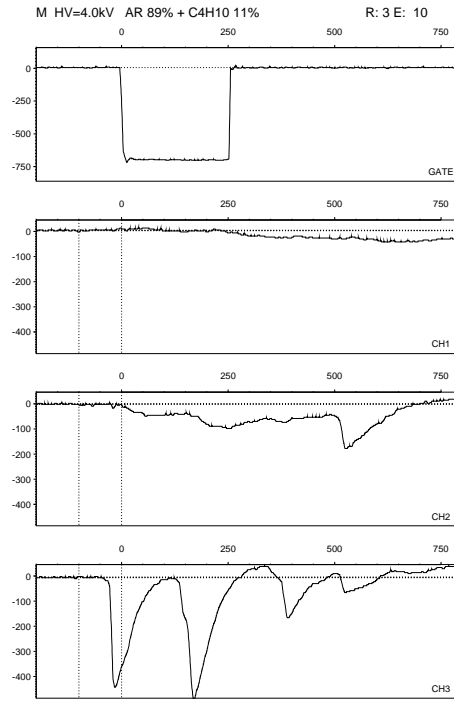


Figure 58: Event with multiple big discharges. Integrated charges: -334 pC, -856 pC, -1069 pC (100 mV/div).

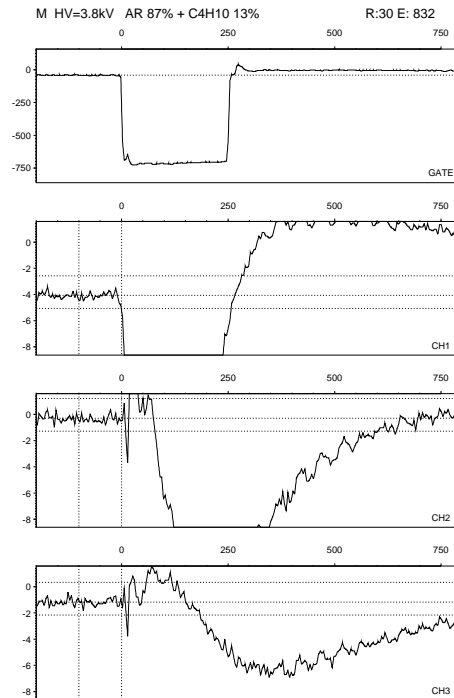


Figure 59: Event with big pulses detected on all three strips (1 mV/div). The first big pulse probably occurred on neighbour strip (which was not read-out). Sharp peaks around $t=0$ (channels 2, 3) are differentiated signal on channel 1 (not to be confused with precursor)

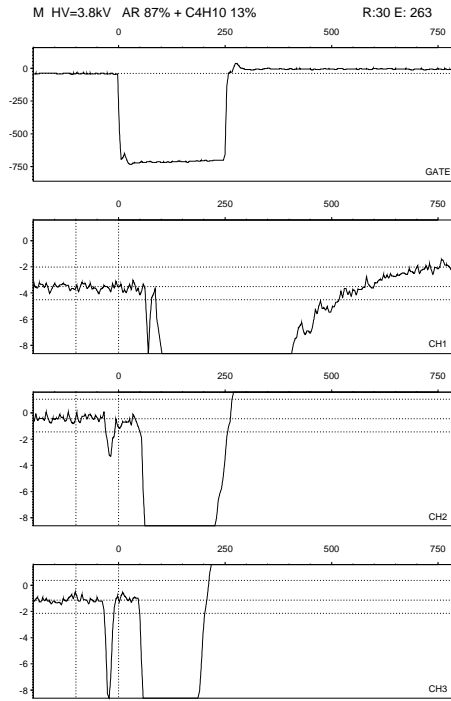


Figure 60: Event with precursor clearly separated from big discharge (channels 2, 3). Two small (integrated charges: -0.8 pC and -2.1 pC) and three big pulses were detected (1 mV/div).

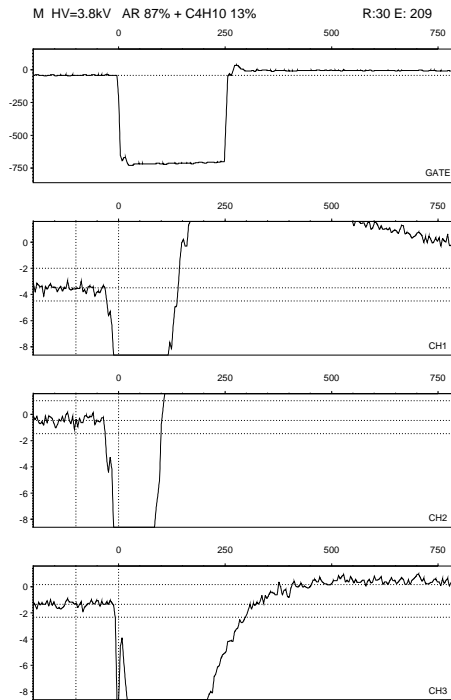


Figure 61: Event with precursor merged with big pulse (channels 1, 2). Three big and no small pulses were detected (1 mV/div).

9.1.2 Big pulse, big pulse with precursor

The shapes of big signals can differ from each other due to possible multiple discharges in the gas gap which last up to few μs . Generally amplitudes are of order of few hundred mV, charge above few tens pC and width greater than few tens ns. In addition a positive signal overshoot can be often observed. A schematic view of big signal is shown in Figure 53. Three cases can be discerned:

- precursor was clearly separated from big signal, its amplitude and charge can be measured by small pulse algorithm
- precursor's signal was merged with big one, and only its amplitude can be measured (as first local minimum below threshold)
- no precursor was observed.

To distinguish big pulse two cuts were applied: amplitude threshold of -2 mV below mean noise level and minimal width of 25 ns.

The big signal which came first was called main big signal and in most cases it had the shortest time duration (usually big discharge was detected on all three strips).

In order to observe small pulses the amplification must be sufficiently high (1 mV/div or 2 mV/div), thus big pulses usually caused underflow (and overflow if positive overshoot occurred). Therefore the amplitude and charge of big and small signals cannot be measured with scope at the same time. Moreover, charges collected with ADC can be underestimated due to overshoots and too short gate (in case of multiple discharges).

An example of event with big pulses is shown in Figure 57 (run with 100 mV/div, without underflows) Multiple discharges can be seen in Figure 58 (100 mV/div). In a typical run (1 or 2 mV/div) big pulse will cause underflow as is shown in event in Figure 59. Events with precursors can be seen in Figures 60 and 61.

It was also observed that main big pulse and main small pulse when both were present did not occur necessarily on the same strip.

9.1.3 Empty event

When neither small nor big signal was detected event was treated as empty. Possibly due to some cross-talks in CAMAC electronics some peaks (even below U_{thr}^- level) can be observed on empty channels around start and end of the gate signal, especially in runs with simultaneous ADC read-out. The averaged "empty pattern" for given run and for each channel can be subtracted and analysis done once again. The small pulses seem not to be affected by this effect because they arrive before the trigger (eg. Figure 56).

9.2 Amplitude and charge resolutions

Accuracies of measured amplitude U and charge Q depend on mean $|U_{noise}|$ value for a given channel. Resolution can be estimated accordingly by $\frac{\Delta U}{U}$ and $\frac{\Delta Q}{Q}$ where $\Delta U = \langle |U_{noise}| \rangle$ and $\Delta Q = \frac{\Delta U \cdot width}{Q \cdot 50\Omega}$, see Figure 62. In general amplitude and charge resolutions were better than 20% as can be seen from Figures 63 and 64 in typical run ($U_{thr}^- = -0.8$ mV).

9.3 Time resolution

All time measurements with scope were done with respect to the trigger arrival time ($t=0$). However, off-line analysis of gate signals showed that -100 mV threshold did not correspond exactly to $t=0$ and dispersion of 0.8 ns occurred. This value in addition to the dispersion of two scintillator signals (2 ns) determines time resolution.

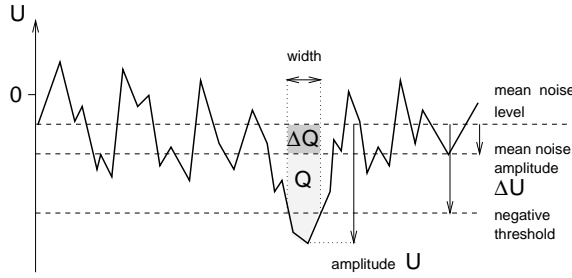


Figure 62: Amplitude and charge resolution of small pulse.

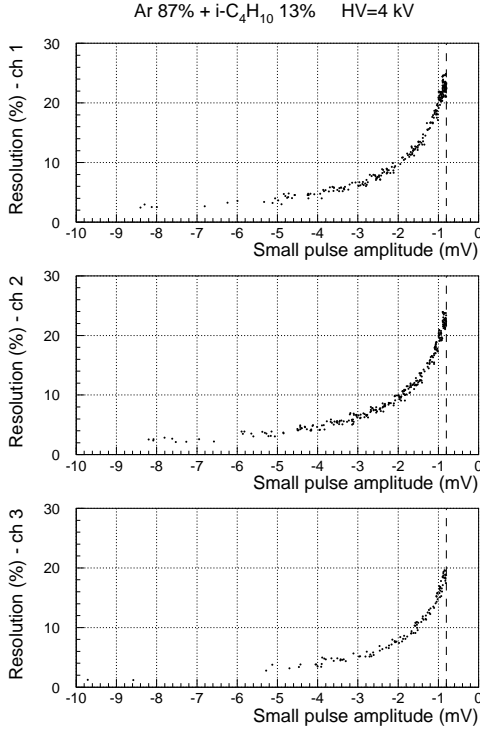


Figure 63: Amplitude resolution in typical run ($U_{\text{thr}}^- = -0.8$ mV).

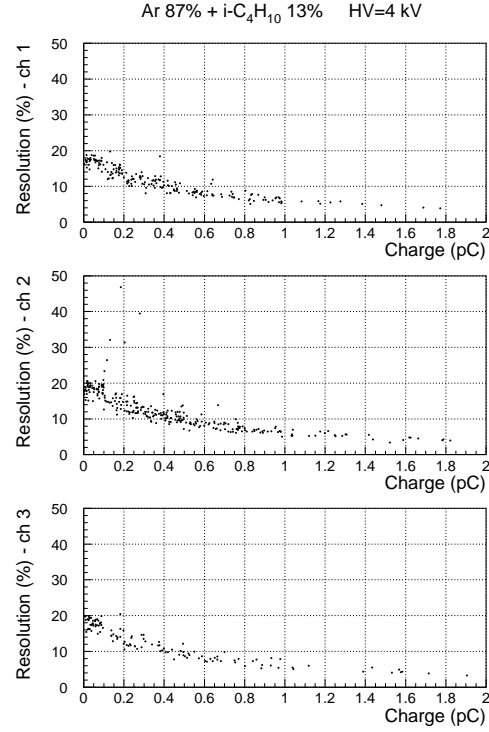


Figure 64: Charge resolution in typical run ($U_{\text{thr}}^- = -0.8$ mV).

9.4 Timing properties of small pulses

As was shown by simulations (compare Figure 33) the development of the fast electron component signal takes about 20 ns. Thus small pulses are expected to arrive in rather narrow time window. The algorithm searched for small pulses within 100 ns time window. An example of arrival time distribution (main small pulses, without big) for argon-isobutane mixture at 4 kV is given in Figure 65 for $U_{\text{thr}}^- = -0.8$ mV. It can be seen that some of events are possibly noise fluctuations. Their charge is relatively small and time is uniformly distributed within time window as is shown in Figure 66.

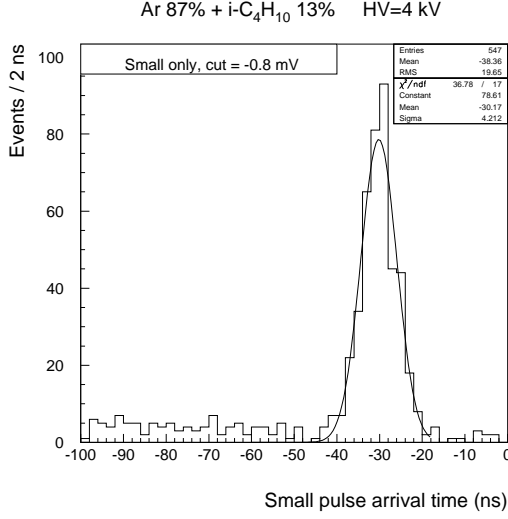


Figure 65: Example of arrival time distribution of small pulse for -0.8 mV cut. Gaussian fit from -60 ns to -20 ns.

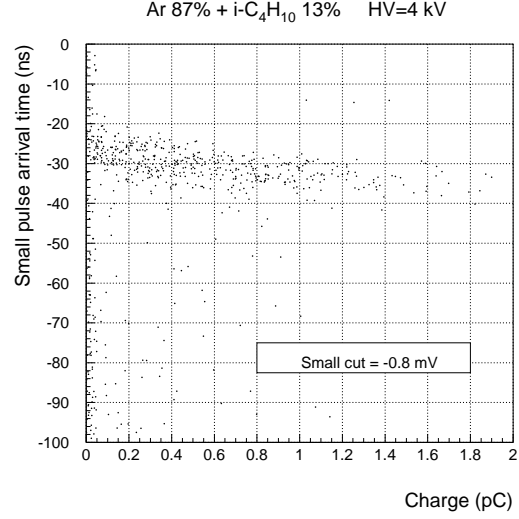


Figure 66: Small pulse arrival time vs charge.

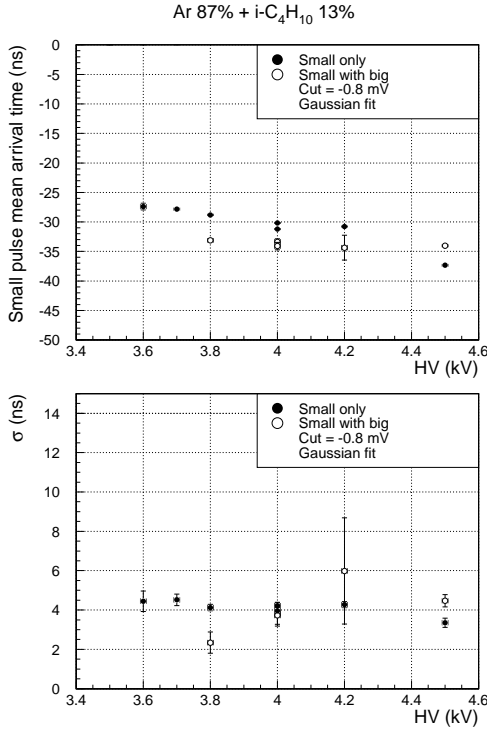


Figure 67: Small pulse mean arrival time and its dispersion (from Gaussian fit) vs the high voltage for argon-isobutane mixture ($U_{\text{thr}}^- = -0.8$ mV).

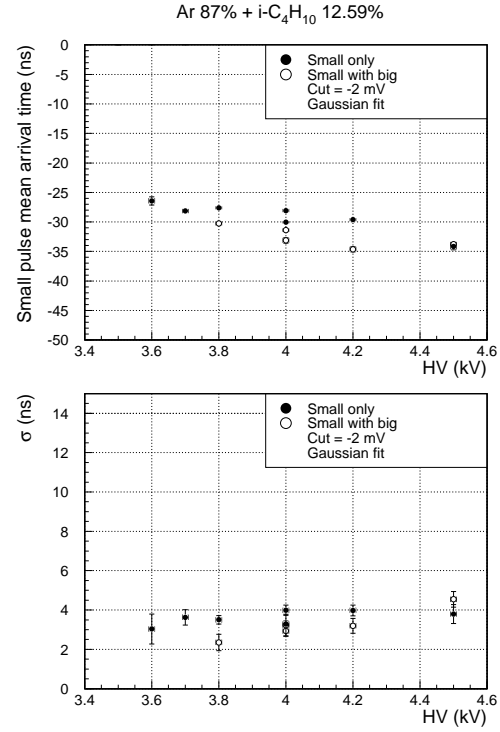


Figure 68: Same as Figure 67 for $U_{\text{thr}}^- = -2$ mV.

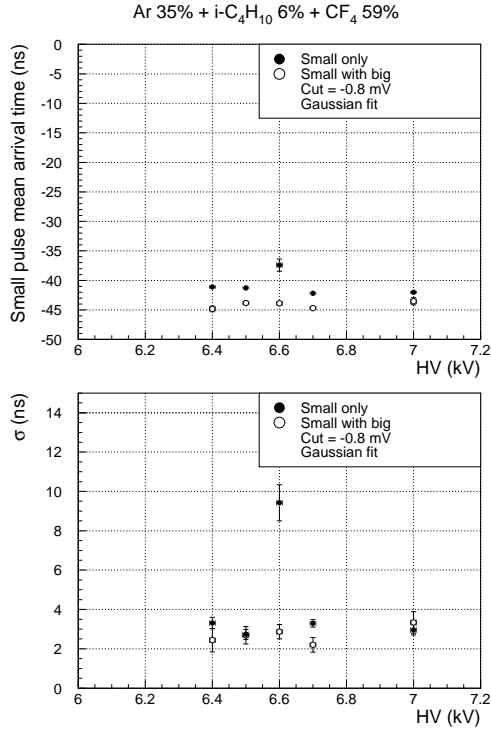


Figure 69: Small pulse mean arrival time and its dispersion (from Gaussian fit) vs the high voltage for argon-isobutane-freon mixture ($U_{\text{thr}}^- = -0.8$ mV).

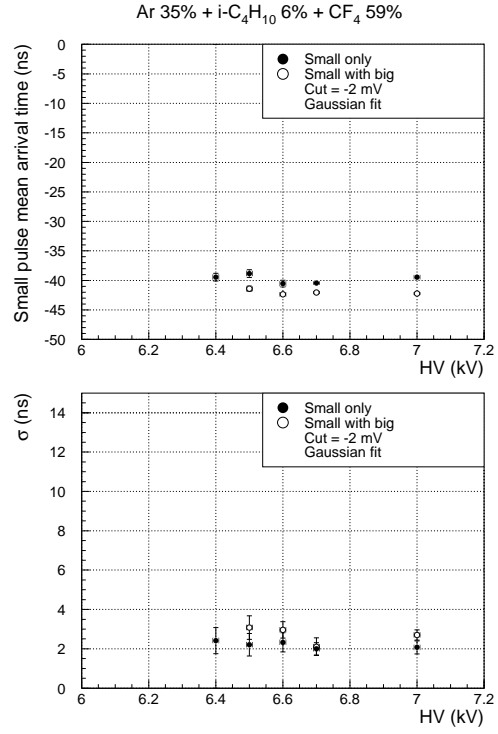


Figure 70: Same as Figure 69 for $U_{\text{thr}}^- = -2$ mV.

In order to measure arrival time of "true" small pulses two methods were applied. In first one, a Gaussian fit was performed from -60 ns to -20 ns (see Figure 65). The results are compared for two U_{thr}^- cuts in Figures 67, 68 for argon-isobutane and in Figures 69, 70 for argon-isobutane-freon mixture. Small pulses with and without big discharges were treated separately (empty and full circles on the plot respectively). This method gave similar results for $U_{\text{thr}}^- = -0.8$ mV, -1 mV and -2 mV⁹. Smaller dispersion can be noticed for argon-isobutane-freon mixture.

⁹The only exception is one point at HV=6.6 kV in Figure 69. Some excess of noise events made Gaussian fit less effective which resulted in shifted mean arrival time and larger dispersion. But this discrepancy vanished for other imposed cuts.

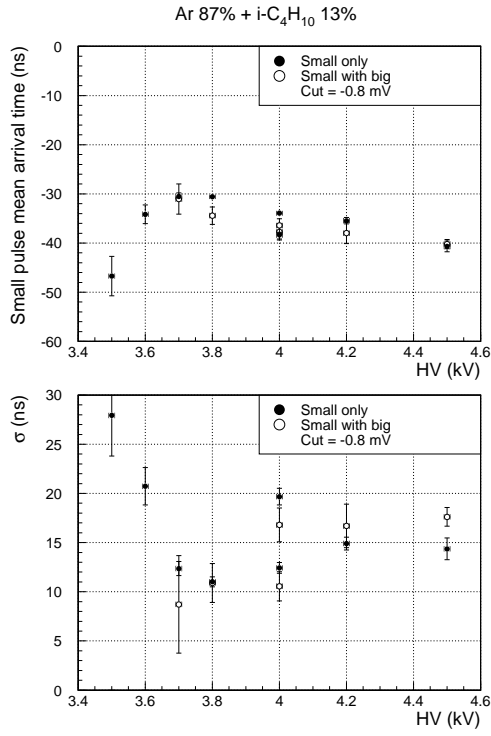


Figure 71: Small pulse mean arrival time and its dispersion vs the high voltage for argon-isobutane mixture. Errors are statistical ($U_{\text{thr}}^- = -0.8$ mV).

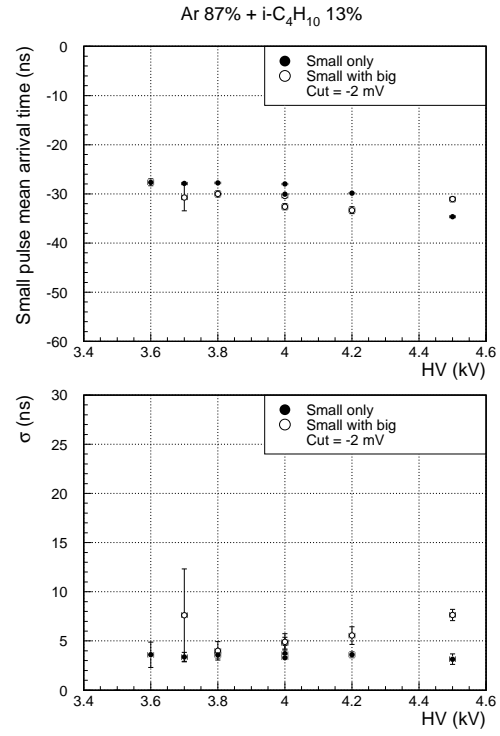


Figure 72: Same as Figure 71 for $U_{\text{thr}}^- = -2$ mV.

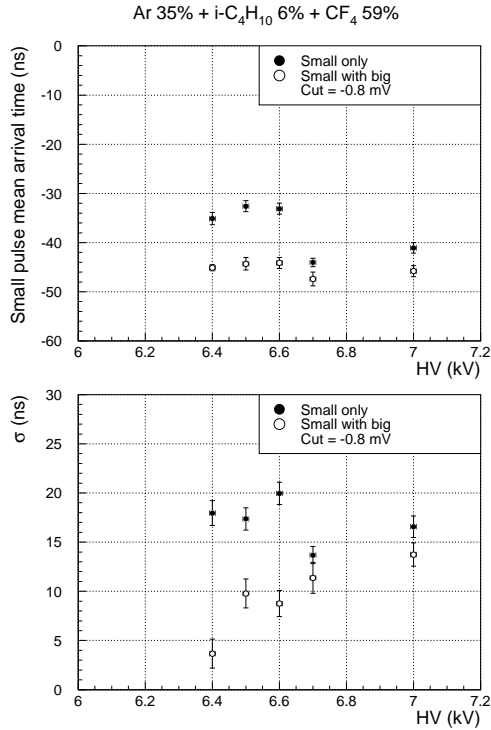


Figure 73: Small pulse mean arrival time and its dispersion vs the high voltage for argon-isobutane-freon mixture. Errors are statistical ($U_{\text{thr}}^- = -0.8$ mV).

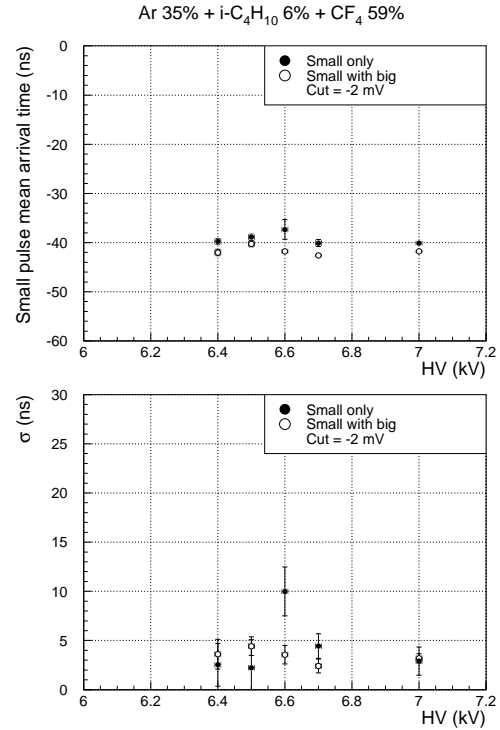


Figure 74: Same as Figure 73 for $U_{\text{thr}}^- = -2$ mV.

In the second method all pulses were used to calculate mean and dispersion. The resulting distributions for two U_{thr}^- cuts can be seen in Figures 71 and 72 for argon-isobutane and in Figures 73 and 74 for argon-isobutane-freon mixtures. In case of $U_{\text{thr}}^- = -0.8$ mV the dispersion was large and the mean value was influenced by noise.

Two methods led to similar results on mean arrival time (for $U_{\text{thr}}^- = -2$ mV). Dispersions obtained by second method were significantly larger for $U_{\text{thr}}^- = -0.8$ mV and -1 mV, but comparable for $U_{\text{thr}}^- = -2$ mV.

The following conclusions can be derived from above results:

- mean arrival time decreased with increasing of the high voltage for the argon-isobutane mixture (but differences occurred between two runs at the "same" conditions, HV=4 kV)
- mean arrival time decreased with increasing of the freon concentration in the argon-isobutane mixture
- differences occurred between arrival time of the small pulses, with and without presence of streamers (in most cases big discharges caused lower mean arrival time)
- in most cases time dispersion was below 5 ns from Gaussian fit (all cuts), and from direct calculation ($U_{\text{thr}}^- = -2$ mV).

The width of small pulses depends on given threshold. An example of width distribution for argon-isobutane mixture is shown in Figure 75 while in Figure 76 an example of width dependence on charge can be seen. Typically the maximal width did not exceed 30 ns and the mean value was below 12 ns.

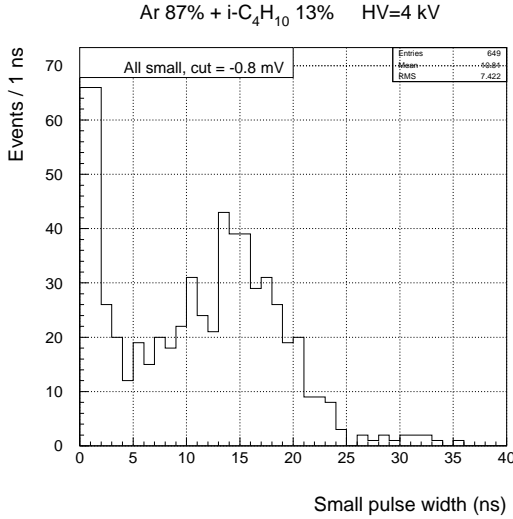


Figure 75: Example of small pulse width distribution for argon-isobutane mixture. Excess of events below 5 ns are caused by noise fluctuations ($U_{\text{thr}}^- = -0.8$ mV).

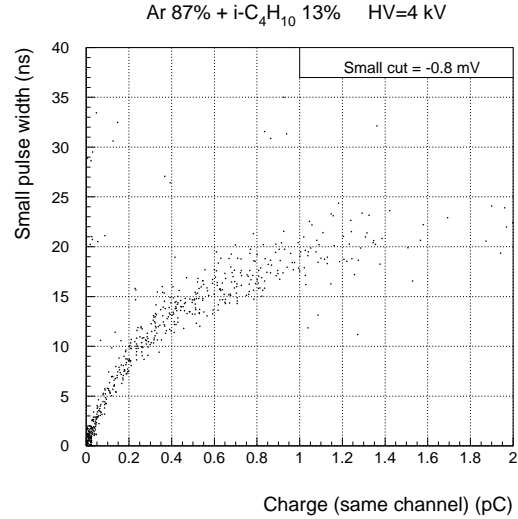


Figure 76: Small pulse width vs its charge on the strip for argon-isobutane mixture.

9.5 Amplitude and charge of small pulses

Amplitude spectra were measured for precursors and small pulses alone. Examples for argon-isobutane mixture ($U_{\text{thr}}^- = -1$ mV) can be seen in Figures 77 and 78 for two HV sets. In the second case streamer mode dominated and precursors with amplitude close to threshold level became frequent. Taking chamber efficiency into account one is particularly interested in detecting

small pulses alone. The resulting spectra for two gas mixtures are shown in Figures 79 and 80 ($U_{thr}^- = -1$ mV, all distributions were normalised to 1). It can be seen that in the studied HV region systematically smaller amplitudes were obtained for argon-isobutane-freon mixture and that amplitude spectra roughly followed exponential distribution. Thus fewer events were lost due to applied U_{thr}^- cut in argon-isobutane mixture.

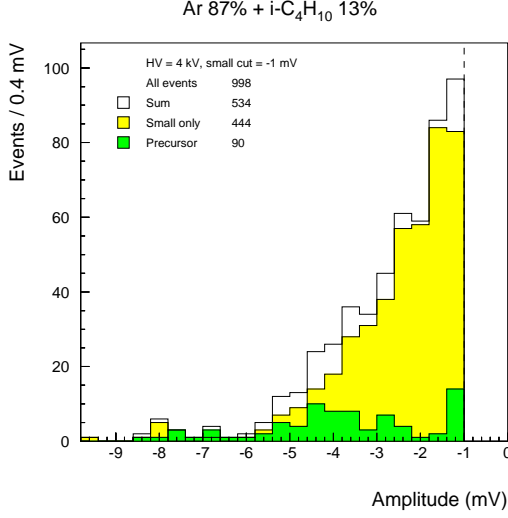


Figure 77: Amplitude distribution of small pulses for argon-isobutane mixture at HV=4 kV ($U_{thr}^- = -1$ mV).

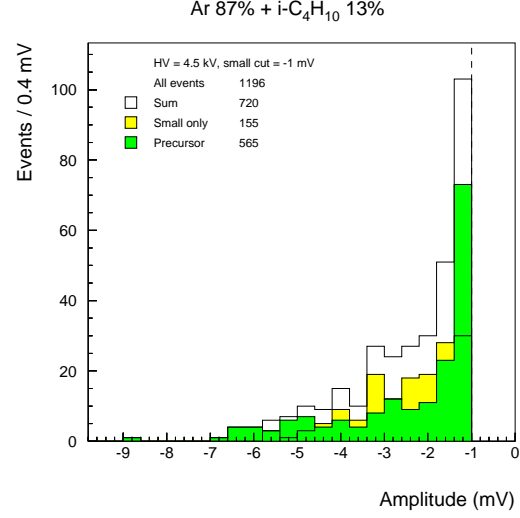


Figure 78: Same as Figure 77 for HV=4.5 kV.

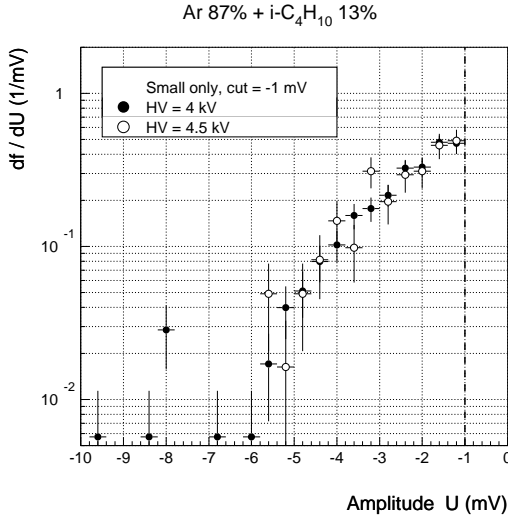


Figure 79: Amplitude distributions of small pulses without big discharges for two HV sets for argon-isobutane mixture ($U_{thr}^- = -1$ mV).

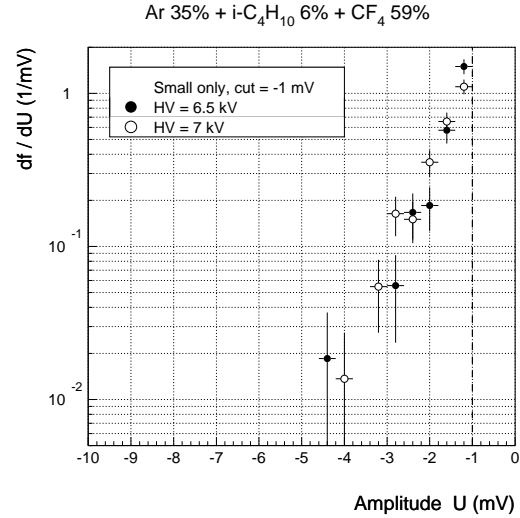


Figure 80: Same as Figure 79 for argon-isobutane-freon mixture.

In order to obtain charge spectra two methods were applied. The first one took into account only strips with detected small pulse and summed their integrated charges. Although this method depended on amplitude threshold it allowed to study charge spectra of small pulses with- and without presence of a streamer. Obtained charge distributions can be compared for two HV sets for argon-isobutane mixture in Figures 81, 82 and for argon-isobutane-freon mixture in Figures 83, 84 ($U_{thr}^- = -1$ mV). In the second gas smaller charges were obtained.

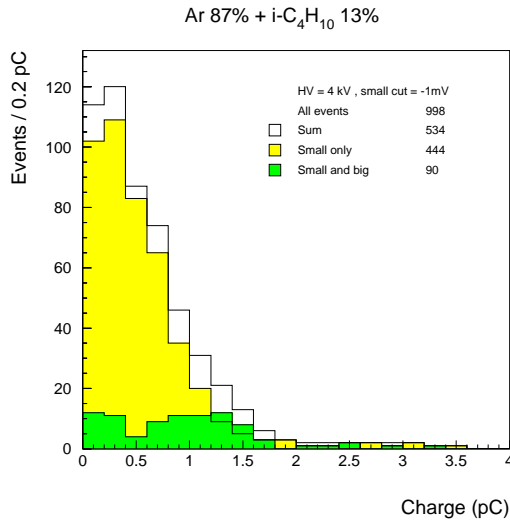


Figure 81: Charge distribution for argon-isobutane mixture at HV=4 kV ($U_{thr}^- = -1$ mV).

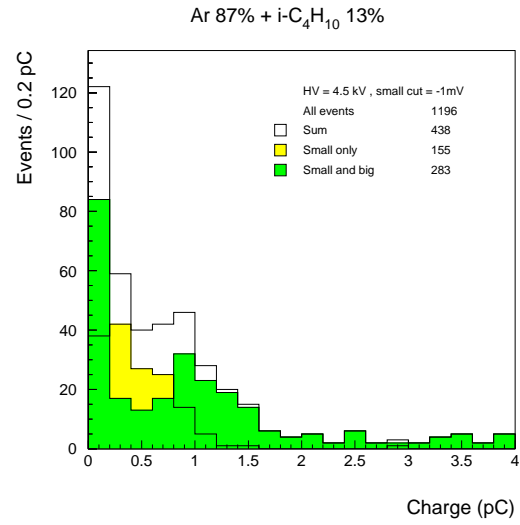


Figure 82: Same as Figure 81 for HV=4.5 kV.

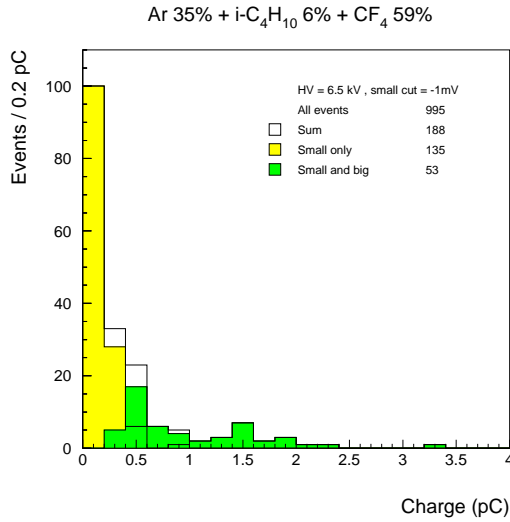


Figure 83: Charge distribution for argon-isobutane-freon mixture at HV=6.5 kV ($U_{thr}^- = -1$ mV).

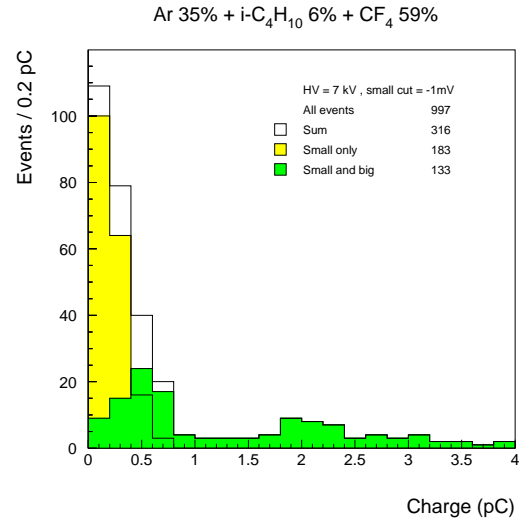


Figure 84: Same as Figure 81 for HV=7 kV.

The integrated charge on a strip depended roughly linearly on pulse amplitude. Typical example is shown in Figure 85 for $U_{thr}^- = -1$ mV.

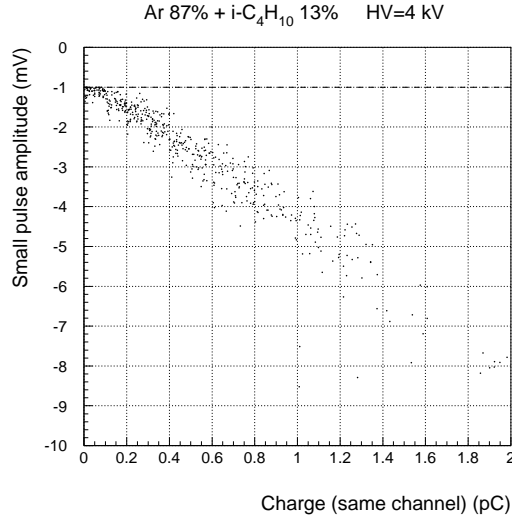


Figure 85: Amplitude of small pulse vs integrated charge on the same strip for $U_{\text{thr}} = -1$ mV.

In the second method, signals on all three strips were integrated over narrow time window (to minimise influence of noise). The integration was performed from -60 ns to 0 ns which was confirmed by arrival time and width distributions of small pulses. Events classified as empty (in the first method) also contributed to the charge distribution, while events with big pulses had to be rejected this time.

The resulting spectra for two HV sets can be seen in Figures 86 and 87 for argon-isobutane and argon-isobutane-freon mixtures respectively (all distributions were normalised to 1). As in the first method in the studied HV region smaller charges were obtained with argon-isobutane-freon.

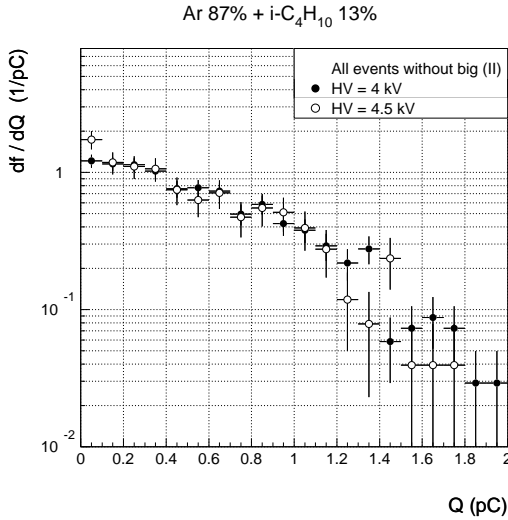


Figure 86: Charge distributions of pulses without streamer (classes: small and empty) for argon-isobutane mixture obtained by second method (see text).

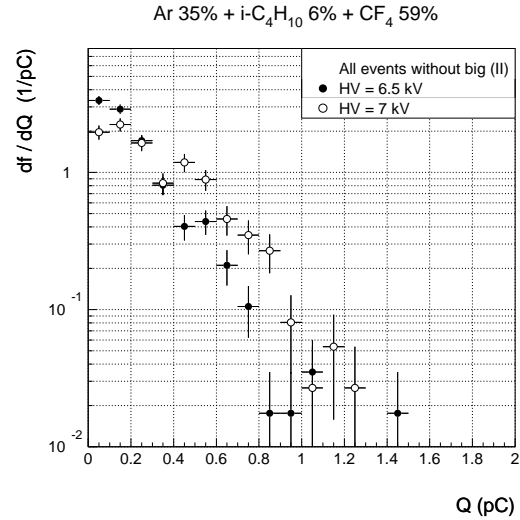


Figure 87: Same as Figure 86 for argon-isobutane-freon mixture.

The mean charge of small pulses without streamer at first exhibited rise with the high voltage and then dropped. It is confirmed by both methods as can be seen from Figures 88 and 89 (except mixture with 59% freon concentration which was still in the region of mean charge rise). At least qualitatively this effect was predicted by simulations made with GARFIELD.

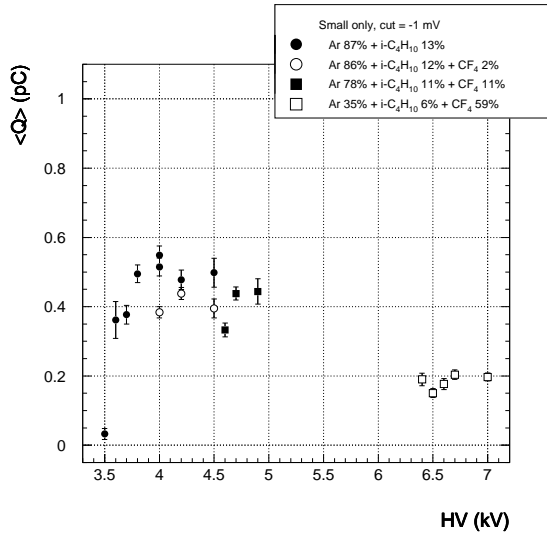


Figure 88: Mean charge of detected small pulses without streamer vs the high voltage from first method for $U_{thr}^- = -1$ mV.

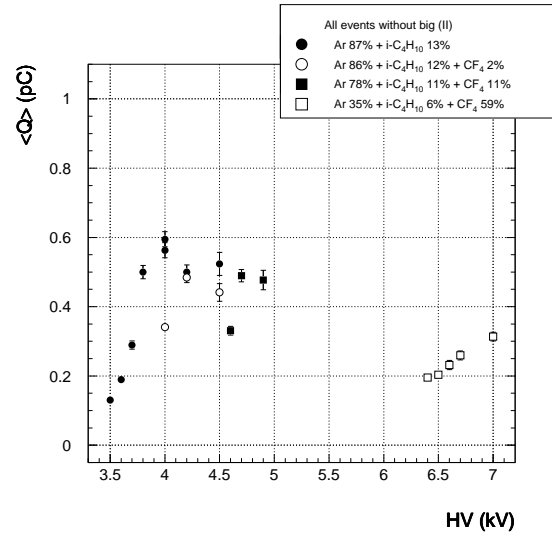


Figure 89: Mean charge of pulses without streamer (classes: small and empty) vs the high voltage from second method.

9.6 Timing properties of big pulses

The arrival time of main big pulses (measured at -2 mV threshold) was spread more widely than in case of small ones. They can start at the same time as small pulses (eg. precursor in Figure 53) or even few hundred nanoseconds after the trigger. The minimal arrival time systematically shortened with increasing freon concentration as well as with increasing the high voltage for every gas composition. Examples of big pulse arrival time distribution are plotted in Figure 90 for argon-isobutane and in Figure 91 for argon-isobutane-freon mixture.

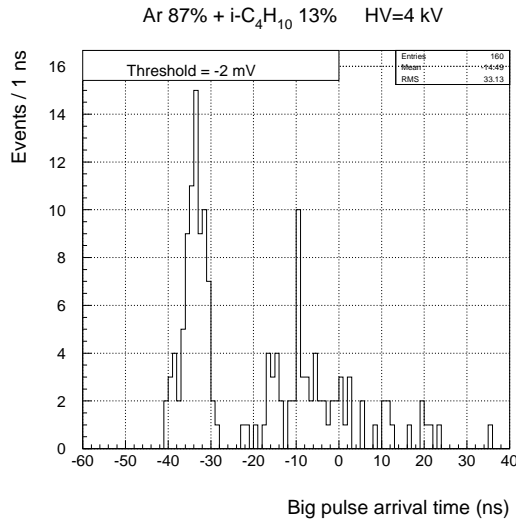


Figure 90: Big pulse arrival time distribution for argon-isobutane mixture at HV=4 kV.

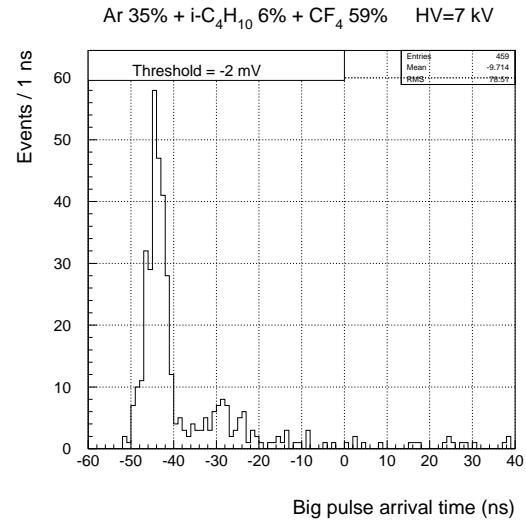


Figure 91: Big pulse arrival time distribution for argon-isobutane-freon mixture at HV=7 kV.

The width of big discharges (at -2 mV threshold) varied from about 30 ns up to values above 800 ns (full time scale). Main big pulses were usually narrower than neighbour ones. For a given mixture a rise of mean width was observed with increasing the high voltage. The minimal width systematically dropped with increasing freon concentration from 100÷80 ns (argon-isobutane) to 30 ns (argon-isobutane-freon). The mean width ranged from 100 to 400 ns. Examples of big pulse width distributions are shown in Figure 92 for argon-isobutane and in Figure 93 for argon-isobutane-freon.

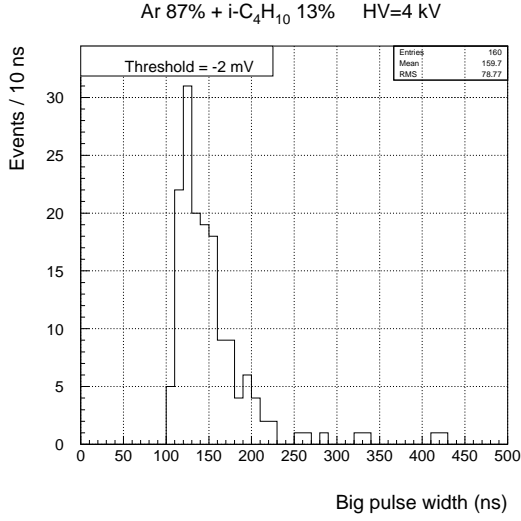


Figure 92: Example of big pulse width distribution for argon-isobutane mixture at HV=4 kV.

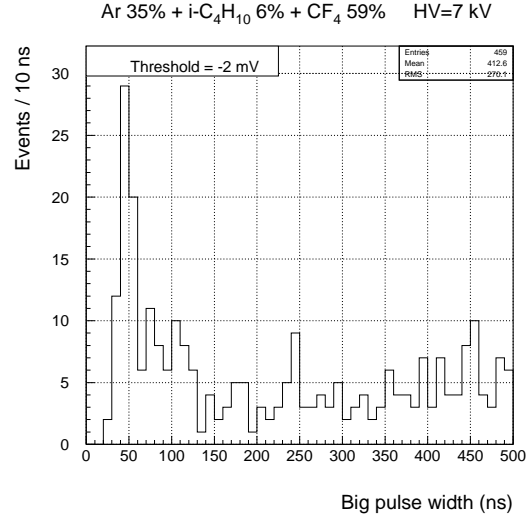


Figure 93: Example of big pulse width distribution for argon-isobutane-freon mixture at HV=7 kV.

The delay between the precursor and the streamer signals was also studied. It was defined as the difference between minimal amplitude (underflow) time and precursor amplitude time, see Figure 53. Only main big pulses were considered and precursor could be either well separated main small pulse (on the same channel, or not, as a big one) or first local minimum (on the same channel).

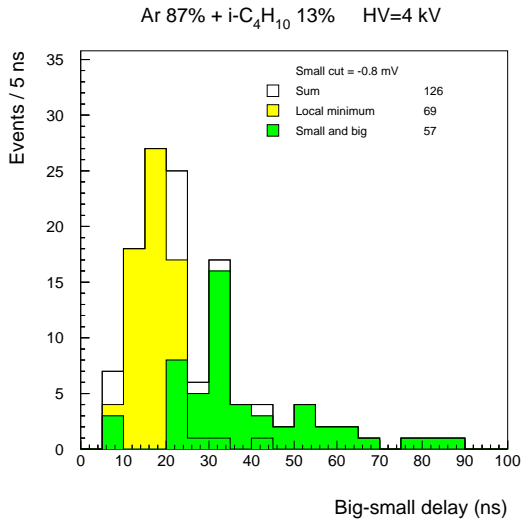


Figure 94: Example of delay distribution between the precursor and the big pulse for argon-isobutane mixture at HV=4 kV.

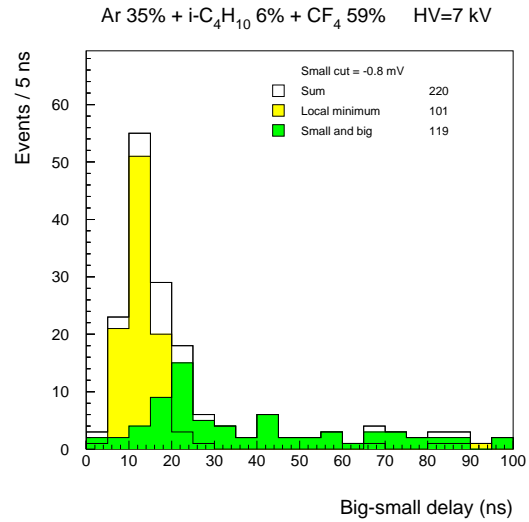


Figure 95: Example of delay distribution between the precursor and the big pulse for argon-isobutane-freon mixture at HV=7 kV.

In Figures 94 and 95 examples of delay distribution are shown for argon-isobutane and argon-isobutane-freon mixtures respectively. As was expected separated small pulses mainly contributed to large values of delay which could exceed 100 ns (eg. Figure 60).

9.7 Strip multiplicity

Small (big) strip multiplicity is the number of strips on which small (big) pulses were detected in single event. The number of detected small pulses, and therefore multiplicity, depends on threshold.

If one considers small events but without big discharge the probability of multiplicity greater than 1 was less than: 10% for $U_{\text{thr}}^- = -2$ mV, 20% for $U_{\text{thr}}^- = -1$ mV and 30% for $U_{\text{thr}}^- = -0.8$ mV (for all gases studied). Strip multiplicities as a function of the high voltage for three cuts are plotted in Figures 96, 98, 100 for argon-isobutane and in Figures 97, 99, 101 for argon-isobutane-freon mixtures.

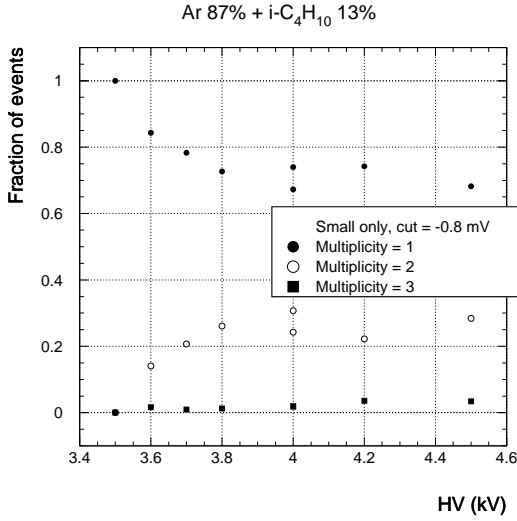


Figure 96: Small pulse strip multiplicities for argon-isobutane mixture ($U_{\text{thr}}^- = -0.8$ mV).

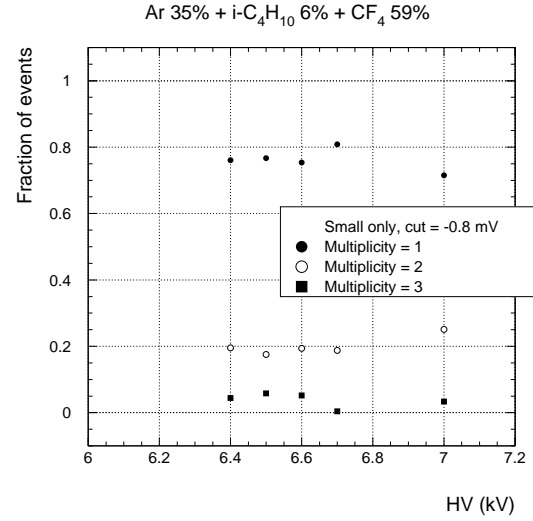


Figure 97: Same as Figure 96 for argon-isobutane-freon mixture ($U_{\text{thr}}^- = -0.8$ mV).

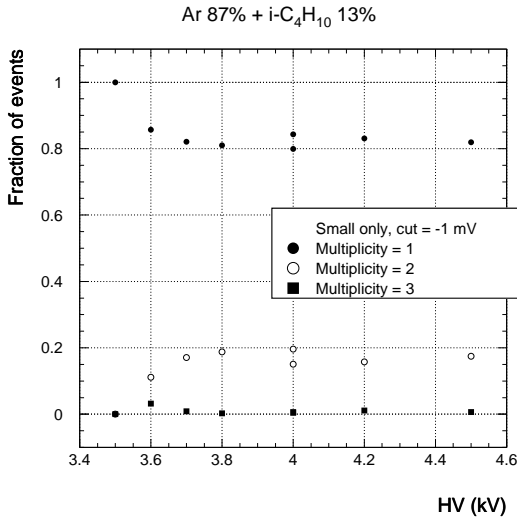


Figure 98: Small pulse strip multiplicities for argon-isobutane mixture ($U_{\text{thr}}^- = -1$ mV).

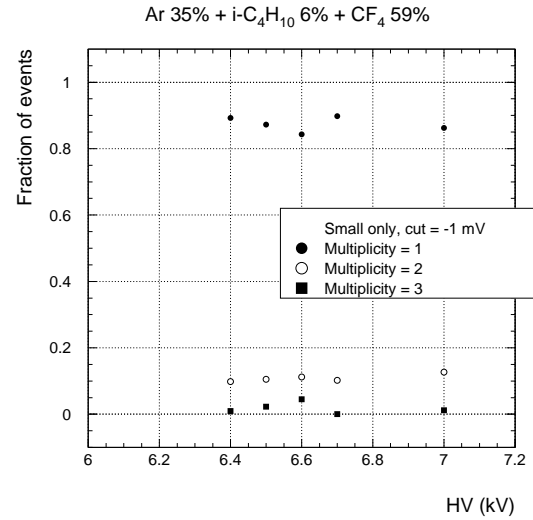


Figure 99: Same as Figure 98 for argon-isobutane-freon mixture ($U_{\text{thr}}^- = -1$ mV).

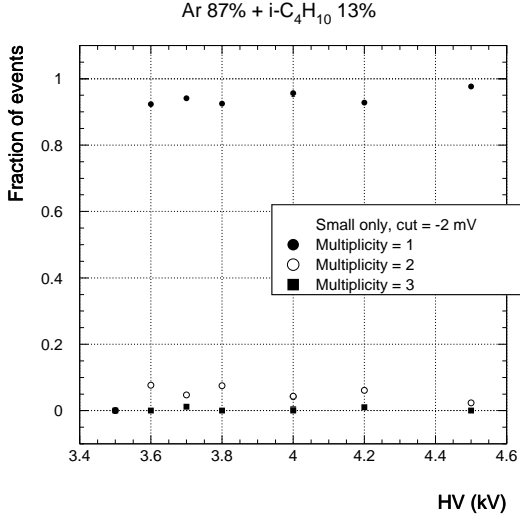


Figure 100: Small pulse strip multiplicities for argon-isobutane mixture ($U_{\text{thr}}^- = -2$ mV).

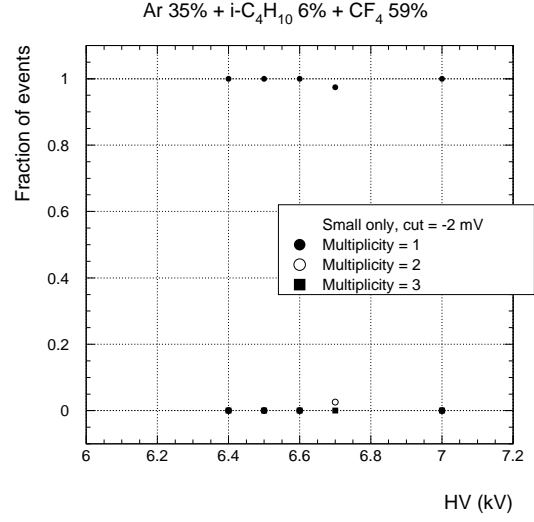


Figure 101: Same as Figure 100 for argon-isobutane-freon mixture ($U_{\text{thr}}^- = -2$ mV).

When main small pulse occurred on channel 1 or 3 the "real" value of multiplicity could be underestimated because only three strips were read-out. Therefore selecting only main small pulses on channel 2 should lead to better results. Differences did not exceed 5% for all three cuts and resulting strip multiplicities for $U_{\text{thr}}^- = -1$ mV are shown in Figures 102 and 103 for argon-isobutane and argon-isobutane-freon mixtures respectively.

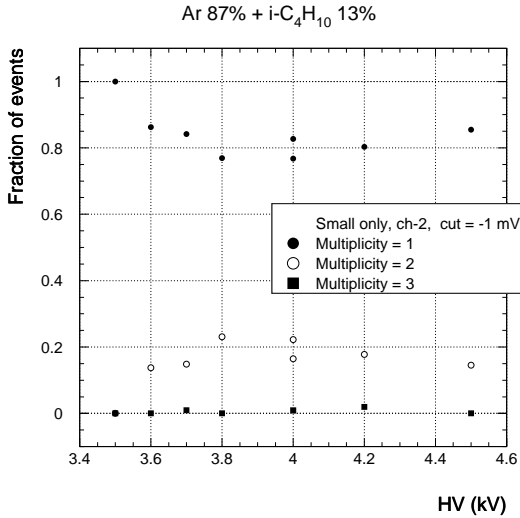


Figure 102: Small pulse strip multiplicities for argon-isobutane mixture for $U_{\text{thr}}^- = -1$ mV. Main big pulse detected on the middle strip (channel 2).

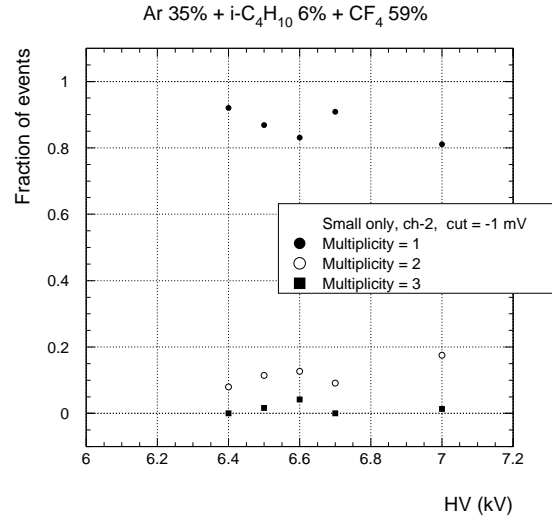


Figure 103: Small pulse strip multiplicities for argon-isobutane-freon mixture for $U_{\text{thr}}^- = -1$ mV. Main big pulse detected on the middle strip (channel 2).

In case of big discharges the probability of strip multiplicity equal to 3 was always above 90%. Big pulse strip multiplicity as a function of the high voltage can be compared in Figures 104 and 105 for argon-isobutane and argon-isobutane-freon mixtures respectively. Simultaneous ADC data for 12 strips showed that big strip multiplicity could be greater than 3. For example in two runs with argon-isobutane mixture at HV=4 kV mean strip multiplicities were found to be 5.2 and 5.4 (20 counts above ADC pedestal which corresponds to 5 pC charge on a strip).

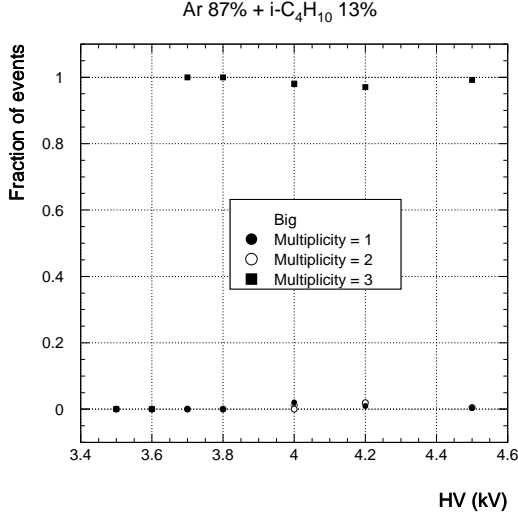


Figure 104: Big pulse strip multiplicity vs the high voltage for argon-isobutane mixture.

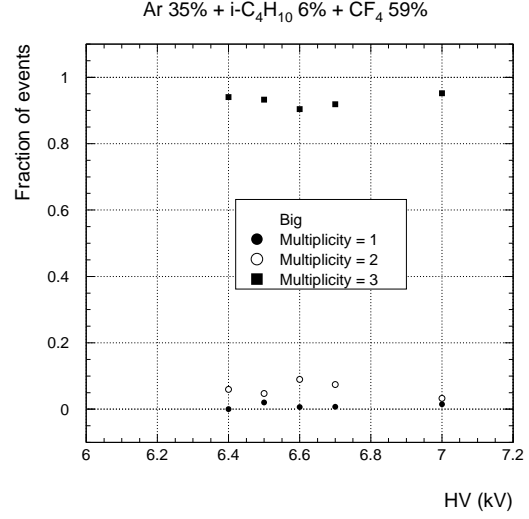


Figure 105: Big pulse strip multiplicity vs the high voltage for argon-isobutane-freon mixture.

It is possible to estimate an area of elementary discharge cell from strip multiplicity of small pulses. It was assumed that:

- every cell has constant dimensions $\sigma \times \sigma$ (each signal has the same charge)
- the centre of each cell is uniformly distributed along x-direction (see Figure 106 for details)
- charges collected on strips are proportional to areas covered by discharge
- amplitude of small signal is proportional to collected charge on the strip.
- dependence of strip multiplicity on threshold may be neglected.

Thus selecting only main small pulses on channel 2 one can estimate cell dimension for 1 cm wide strips by

$$\sigma = \frac{N_2}{N_1 + N_2} \cdot 1 \text{ cm}$$

where

- N_1 – number of events with multiplicity = 1
- N_2 – number of events with multiplicity ≥ 2 .

The resulting cell widths σ can be compared for two U_{thr}^- cuts in Figures 107 and 108 for all gases studied.

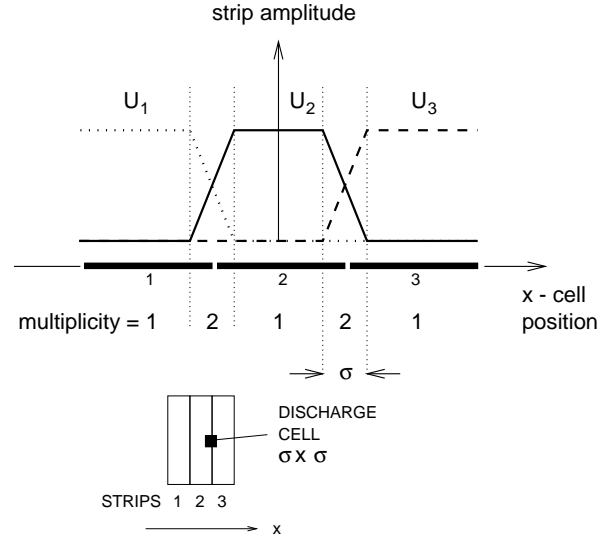


Figure 106: Estimation of elementary discharge cell.

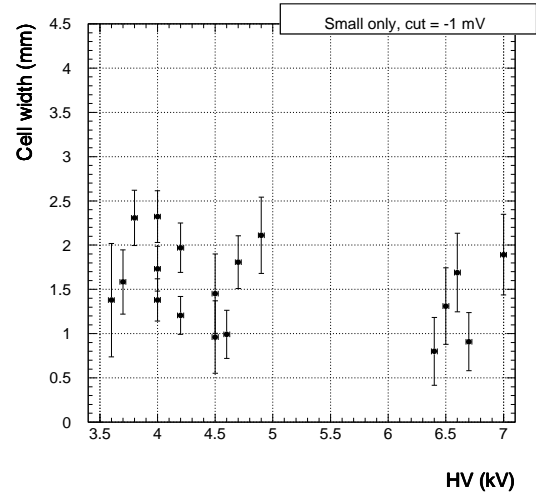
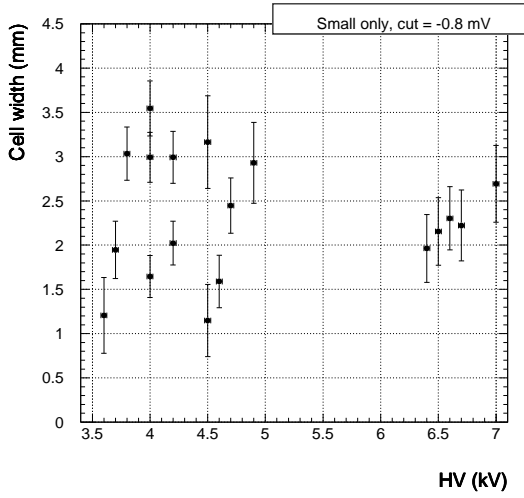


Figure 107: Estimated width of the discharge cell vs the high voltage for all gas mixtures and -0.8 mV cut. Errors are statistical.

Figure 108: Same as Figure 107 for -1 mV cut.

9.8 Efficiency

Efficiency of each run was defined as

$$\varepsilon = \frac{N_{big} + N_{small}}{N_{big} + N_{small} + N_{empty}}$$

where

- N_{big} – number of events with big pulse(s)
- N_{small} – number of events with small pulse(s) only
- N_{empty} – number of empty events.

In Figures 110 and 109 the efficiency is shown as a function of the high voltage obtained for three U_{thr}^- cuts: -0.8 mV, -1 mV and -2 mV for all gases. Generally ε was limited to 85% (with statistical error $<5\%$), but full scale of the high voltage has not been studied.

With increasing freon concentration the HV working point had to be increased also in order to obtain the same efficiency level. Difference of about 3 kV occurred between 0% and 59% freon concentration.

The contribution of big discharges to the efficiency defined as

$$\varepsilon_{big} = \frac{N_{big}}{N_{big} + N_{small} + N_{empty}}$$

can be also treated as streamer probability. Its value grows with the high voltage as well, which can be seen from Figure 112.

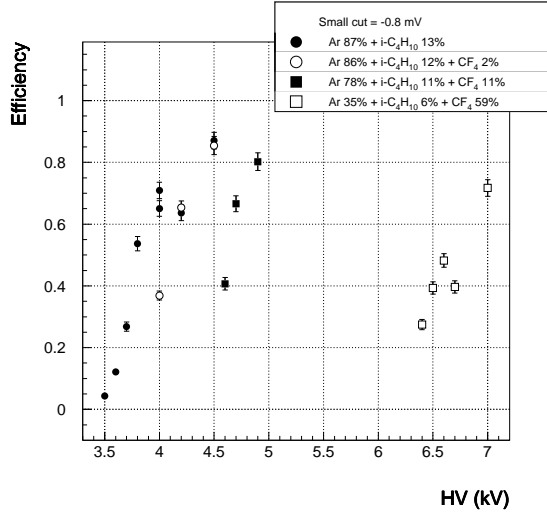


Figure 109: Efficiency vs the high voltage for $U_{thr}^- = -0.8$ mV. Errors are statistical.

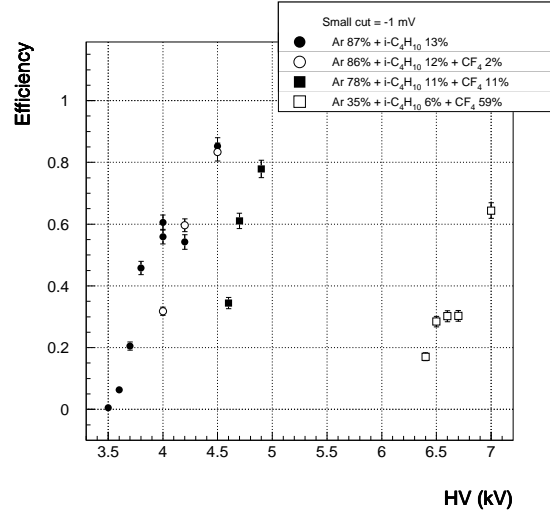


Figure 110: Efficiency vs the high voltage for $U_{thr}^- = -1$ mV. Errors are statistical.

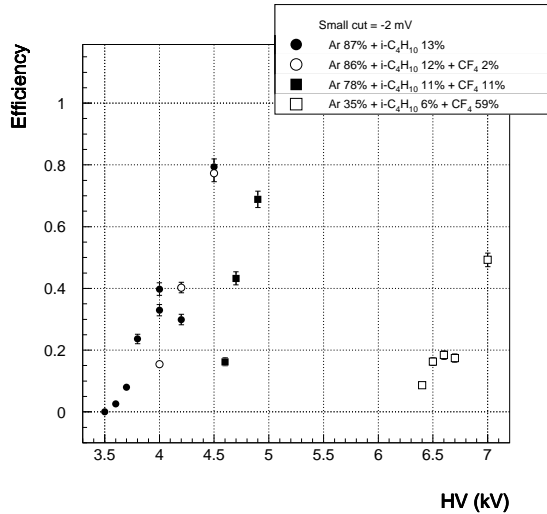


Figure 111: Efficiency vs the high voltage for $U_{thr}^- = -2$ mV. Errors are statistical.

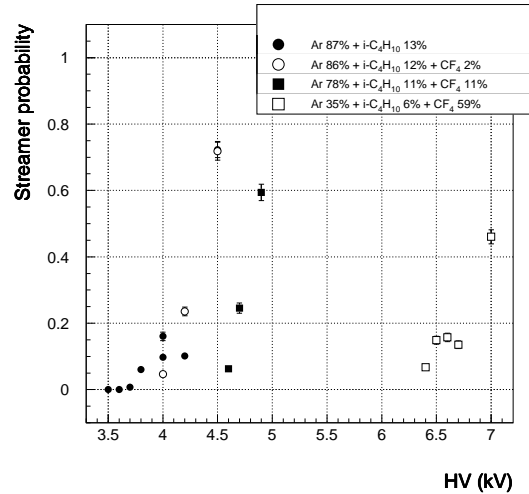


Figure 112: Streamer probability vs the high voltage. Errors are statistical.

It should to be stated that the efficiency discussed above must be corrected for some geometrical effects. The width of scintillator plates (3.5 cm) was somewhat wider than the width of three central strips (3 cm) and two scintillators could be also displaced. In two additional runs (with same gas and HV) strips 8, 9, 10 (normal mode) and 7, 9, 11 (test mode) were read-out with scope. Figure 113 compares number of small pulses detected on each strip independently. Analogous plot for big pulses is shown in Figure 114. It can be seen that up to 5-6 % of small events cannot be detected in normal mode (varying probability of multiplicity greater than 1 from 0% to 20%). Data collected with ADC show that there is no need of such correction for big pulses (20 counts above ADC pedestal which corresponds to 5 pC charge on a strip). When big pulses were not observed on strips 8, 9, 10 there were no big pulses on the other strips either.

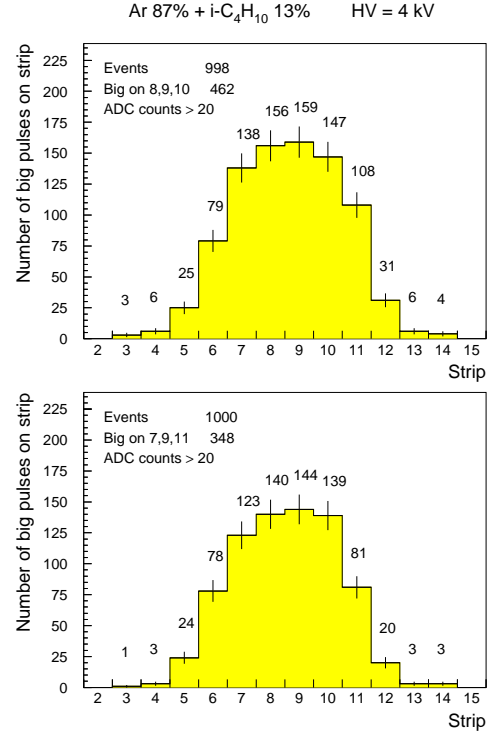
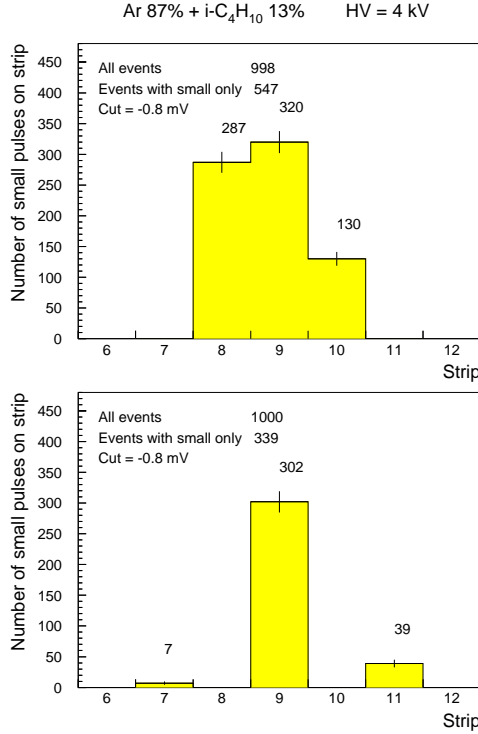


Figure 113: Number of small pulses detected on each strip independently in normal run (top) and in test run (bottom). Data collected with scope for $U_{thr}^- = -0.8$ mV.

Figure 114: Number of big pulses detected independently on each strip in normal run (top) and in test run (bottom). Data collected with ADC. 20 counts above pedestal (5 pC) were required for detecting big pulse on a strip.

Simulation of cosmic rays passed through the detector system showed that expected losses in efficiency due to purely geometric effects were: 2% for ideal scintillators positioning and 2÷5% when 0.5 cm scintillator displacements were allowed.

10 Comparison between simulation and experiment

The instantaneous results obtained with GARFIELD can not be directly compared to those measured experimentally because signal pick-up mechanism has to be taken into consideration.

The following effects observed experimentally were predicted by simulations:

1. Difference of about 2.5 kV for transition points between avalanche and streamer mode of operation for argon-isobutane and argon-isobutane-freon mixtures
2. Better time resolution and faster signal arrival time for argon-isobutane-freon mixture
3. Decrease of mean visible charge in avalanche mode when streamer probability becomes significant

The major discrepancies are listed below:

1. In the avalanche mode, mean charges smaller than those predicted by simulation were measured, even after decreasing simulated charge by a factor of 2 due to signal pick-up. Many factors may lead to this discrepancy, eg. uncertainty of the Townsend coefficient and gas composition, neglecting space charge effect at higher gains.
2. Measured slopes of streamer probability curves were smaller than those from simulation. This means that simple condition for streamer formation ($\alpha x > 20$) was not adequate.
3. Intrinsic time resolution of $\sigma \approx 2$ ns was obtained from simulation (argon-isobutane). Experimental data were close to: $\sigma \approx 4$ ns for argon-isobutane and $\sigma \approx 2$ ns for argon-isobutane-freon. This may be explained by the additional dispersion of coincidence signals from two scintillators used for triggering of the chamber.

11 Conclusions

The following conclusions on detector performance and future investigations can be derived from measurements and simulations:

1. Simulations has shown that about 60% of the charge from fast electron component is available for detection (mainly due to capacitances of gas and electrodes). After applying signal threshold ($U_{\text{thr}}^- = -1$ mV, -2 mV) this ratio decreases to about 40%.
2. Efficiency was limited by a noise level of strip signals. In the region where spark probability was less than 10%, the efficiency in avalanche mode do not exceed 55–25% (depending on the U_{thr}^-). The rise of the signal amplitude U_0^{max} can be achieved by reduction of strip capacitance C_0 . This may improve the efficiency for the same U_{thr}^- cut. If the observed noise was mainly due to connecting cables and CAMAC electronics, mounting of the pre-amplifiers directly on the strips should improve efficiency.
3. The gas system was not stable in time, causing the differences between data taken with "same" mixture and HV set. The gas volume of the tested chamber was very small (80 cm^3) and the gas flow was kept below $2 \text{ dm}^3/\text{h}$. Because used flowmeters were suitable for larger detector systems, a minimal variation of flowmeter indication led to $\sim 1\%$ difference in concentration of mixture components (the effect which is remarkable). In addition the possible effect of gas impurities should be taken into account.

4. Mean strip multiplicity for 1 cm wide strips was small in the avalanche mode, namely 1.1–1.4 (depending on the applied threshold). Simulation showed that amplitude of signal induced on strip depend on position of the discharge in the chamber.
On the contrary, almost always streamers caused hits on more than 3 strips.
5. Time resolution below 4 ns was achieved in avalanche mode for externally triggered chamber. Simulation predicts resolution better than 2 ns.

Acknowledgements

I would like to thank warmly my supervisors, prof. Jan Królikowski and dr Maciej Górski, for their inestimable help in preparation of this thesis. Their experience and knowledge as well as many valuable discussions and helpful suggestions were highly appreciated.

I also acknowledge dr S.F.Biagi for providing the recent MAGBOLTZ code.

Special thanks are addressed to the members of the Detector Laboratory of the Institute of Experimental Physics for construction of the RPC prototype and for technical support during testing the chamber.

I am also grateful to all members of the Warsaw CMS group and people from other collaborations for their useful hints and remarks.

References

- [1] R. Santonico, *RPC: Status and Perspectives*, proceedings of the II International Workshop on The Resistive Plate Chambers in Particle Physics and Astrophysics, Pavia, Italy, June 1993.
- [2] *The Large Hadron Collider, Conceptual Design*, CERN/AC 95-05, October 1995.
- [3] *The Compact Muon Solenoid - Technical Proposal*, CERN/LHCC 94-38, December 1994.
- [4] T. Yamashita et al., *Measurements of the electron drift velocity and positive-ion mobility for gases containing CF₄*, NIM A 283 (1989) 709.
- [5] G. Schultz et al., *Mobilities of positive ions in some gas mixtures used in proportional and drift chambers*, Rev. Phys. Appl. 12 (1977) 67.
- [6] F. F. Rieke, W. Prepejchal, *Ionisation cross sections of gaseous atoms and molecules for high-energy electrons and positrons*, Phys. Rev. A6 (1972) 1507.
- [7] G. Malamud et al., *Specific primary Ionisation induced by minimum ionising electrons in CH₄, C₂H₆, C₃H₈, i-C₄H₁₀, argon, dimethylether, triethylamine, and tetrakis(dimethyloamino)ethylene*, J. Appl. Phys. 74 (1993) 3645.
- [8] H. Fischle et al., *Experimental determination of ionisation cluster size distributions in counting gases*, NIM A301 (1991) 202.
- [9] F. Lapique, F. Piuz, *Simulation of the measurement by primary cluster counting of the energy lost by a relativistic ionising particle in argon*, NIM 175 (1980) 297.
- [10] F. Sauli, *Principles of operation of multiwire proportional and drift chambers*, CERN 77-09.
- [11] A. Peisert, F. Sauli, *Drift and diffusion of electrons in gases: a compilation*, CERN 84-08.
- [12] R. Veenhof, *Garfield, a drift chamber simulation program, User's guide, Version 5.16*, CERN Program Library, entry W5050.
- [13] A. Sharma, F. Sauli, *First Townsend coefficient measured in argon based mixtures at high fields*, NIM A334 (1993) 420.
- [14] A. Arefiev et al., RD5 collab., *A measurement of the First Townsend coefficient in CF₄, CO₂ and CF₄/CO₂ mixtures at high, uniform electric field*, CERN-PPE/93-82.
- [15] Private communications from S. F. Biagi, author of MAGBOLTZ; S. F. Biagi, *A multiterm Boltzmann analysis of drift velocity, diffusion, gain and magnetic-field effects in argon - methane - water-vapour mixtures*, NIM A 283 (1989) 716.
- [16] I. Smirnov, *HEED, an ionisation loss simulation program, User's guide, Version 1.00*, CERN Program Library, entry W5060.
- [17] H. Raether, *Electron avalanches and breakdown in gases*, Butterworth, London, 1964.
- [18] P. Fonte, *A model of breakdown in parallel-plate detectors*, IEEE NS-symposium, 1994.